Commun. Comput. Phys.
doi: 10.4208/cicp.OA-2018-0049

Vol. **26**, No. 2, pp. 346-388
August 2019

Numerical Modeling of Non-Isothermal Compositional Compressible Gas Flow in Soil and Coupled Atmospheric Boundary Layer

Ondřej Pártl[1,*], Michal Beneš[1], Radek Fučík[1] and Tissa Illangasekare[2]

[1] *Faculty of Nuclear Sciences and Physical Engineering, Czech Technical University in Prague, Trojanova 13, 120 00 Prague 2, Czech Republic.*
[2] *Center for the Experimental Study of Subsurface Environmental Processes, Department of Civil and Environmental Engineering, Colorado School of Mines, Golden, CO 80401, Colorado, USA.*

Communicated by Kun Xu

Received 19 February 2018; Accepted (in revised version) 18 June 2018

Abstract. Compositional gas flow in a heterogeneous porous medium and in the coupled atmospheric boundary layer above the porous medium surface is of interest in many applications, which requires reliable numerical tools for modeling of very complex physical processes. But there are still many important effects which are very often ignored in contemporary models of this flow. One of them is compressibility. So far, no models of non-isothermal compositional compressible gas flow in a porous medium and in the coupled atmospheric boundary layer above its surface has been reported in the literature. Therefore, we propose mathematical and numerical models for the description of the above scenario. In order to assess the reliability of our numerical model, we analyze its convergence by quantitative computational studies. We also present several qualitative computational studies which present the dynamics of the non-isothermal compositional compressible gas flow in free flow–porous medium flow interaction.

AMS subject classifications: 76N99, 76S99

Key words: Compressible flow, non-isothermal flow, compositional flow, porous medium, free flow, coupling conditions.

Nomenclature

Greek letters

α_{BJ} Beavers-Joseph coefficient $[-]$ (introduced in (2.39), page 355)

*Corresponding author. *Email addresses:* ondrej.partl@fjfi.cvut.cz (O. Pártl), michal.benes@fjfi.cvut.cz (M. Beneš), radek.fucik@fjfi.cvut.cz (R. Fučík), tillanga@mines.edu (T. Illangasekare)

α_{EOC} coefficient defined on page 372
$\Gamma^{\alpha}_{i,j}$ side of V_i^{α} (defined on page 361)
$\Gamma_{f,\theta}$ part of $\partial\Omega^{pm}$, where $\theta \in \{\mathrm{Dir}, \mathrm{Neu}, \mathrm{out}\}$ and $f \in \{p, X_n, T\}$
Γ^{ff}_{θ} part of $\partial\Omega^{ff}$, where $\theta \in \{\mathrm{left}, \mathrm{right}, \mathrm{top}_1, \mathrm{top}_2, \mathrm{side}\}$
Γ_i, Γ^b_i parts of ∂V_i (defined on page 357)
$\Gamma^e_{i,j}$, $\Gamma^b_{i,j}$ parts of ∂V_i (defined on page 357)
Γ^{pm}_{θ} part of $\partial\Omega^{pm}$, where $\theta \in \{\mathrm{wall}, \mathrm{gap}_1, \mathrm{gap}_2, \mathrm{right}\}$
$\delta_{i,j}$ Kronecker delta
κ ratio of specific heats $[-]$
λ thermal conductivity $[\mathrm{kg}\cdot\mathrm{m}\cdot\mathrm{s}^{-3}\cdot\mathrm{K}^{-1}]$
Λ^e, Λ_i sets of indices (defined on page 357)
Λ^e_i, Λ^b_i sets of indices (defined on page 357)
$\Lambda_{i,j}$, Λ^n_i sets of indices (defined on page 357)
$\Lambda^b_{f,\theta,i}$ set of indices related to function f, where $\theta \in \{\mathrm{Neu}, \mathrm{out}\}$ (defined on page 357)
μ dynamic viscosity $[\mathrm{kg}\cdot\mathrm{m}^{-1}\cdot\mathrm{s}^{-1}]$
ν output time step [s] (introduced in (4.4), page 372)
ρ density $[\mathrm{kg}\cdot\mathrm{m}^{-3}]$
τ time step in the numerical scheme from Section 3.1 [s]
τ_{cou} time step for the coupling of the numerical schemes from Section 3 [s]
ϕ porosity $[-]$
φ_i basis function associated with node x_i of $\mathcal{T}$
Ω spatial domain
$\tilde{\Omega}^{ff}$ extension of Ω^{ff} (defined on page 360)

Latin letters

a longitudinal dispersion coefficient [m]
c_p specific heat at constant pressure $[\mathrm{m}^2\cdot\mathrm{s}^{-2}\cdot\mathrm{K}^{-1}]$
$c_{p,\sigma}$ specific heat at constant pressure of component σ $[\mathrm{m}^2\cdot\mathrm{s}^{-2}\cdot\mathrm{K}^{-1}]$
c_s specific heat capacity of the solid matrix $[\mathrm{m}^2\cdot\mathrm{s}^{-2}\cdot\mathrm{K}^{-1}]$
c_V specific heat at constant volume $[\mathrm{m}^2\cdot\mathrm{s}^{-2}\cdot\mathrm{K}^{-1}]$
$c_{V,\sigma}$ specific heat at constant volume of component σ $[\mathrm{m}^2\cdot\mathrm{s}^{-2}\cdot\mathrm{K}^{-1}]$
D diffusion coefficient $[\mathrm{m}^2\cdot\mathrm{s}^{-1}]$
$D_{\sigma,\gamma}$ multicomponent diffusion coefficient $[\mathrm{m}^2\cdot\mathrm{s}^{-1}]$
D_n diffusion coefficient of the NAPL vapor $[\mathrm{m}^2\cdot\mathrm{s}^{-1}]$

$\boldsymbol{d}_\sigma$	diffusion driving force of component σ $[\mathrm{m}^{-1}]$
e	specific energy $[\mathrm{m}^2\cdot\mathrm{s}^{-2}]$
F	sink/source term of the mixture $[\mathrm{kg}\cdot\mathrm{m}^{-3}\cdot\mathrm{s}^{-1}]$
f_i^α, $f_{i,j}^\alpha$	functions related to $\boldsymbol{x}_i^\alpha$ and $\boldsymbol{x}_{i,j}^\alpha$, respectively (defined on page 361)
$\underline{f_{i,j}^\alpha}$	upwind term defined by (3.20), page 362
f_B^e	function related to $\boldsymbol{x}_B^e$ (defined on page 357)
$\dot{f}$	time derivative of f, where $f=f(t)$
f_e	function related to T^e (defined on page 357)
f_i, $f_{i,j}$	functions related to $\boldsymbol{x}_i$ and $\boldsymbol{x}_{i,j}$, respectively (defined on page 357)
$f_{i,j}^e$, $f_{i,j}^b$	functions related to $\boldsymbol{x}_{i,j}^e$ and $\boldsymbol{x}_{i,j}^b$, respectively (defined on page 357)
$\underline{f_{i,j}^{e,n+1}}$	upwind term defined by (3.7), page 359
f^n	value of f at time t_n (defined on page 357)
F_n	sink/source term of the NAPL vapor $[\mathrm{kg}\cdot\mathrm{m}^{-3}\cdot\mathrm{s}^{-1}]$
$\boldsymbol{g}$	gravitational acceleration vector $[\mathrm{m}\cdot\mathrm{s}^{-2}]$
h, h_{x_1}, h_{x_2}	spatial mesh parameters introduced in Section 4.1 [m]
$\boldsymbol{I}$	identity tensor
$\mathcal{I}$	interface between Ω^{pm} and Ω^{ff}
$\boldsymbol{k}$	permeability tensor $[\mathrm{m}^2]$
$\tilde{k}$, $\tilde{k}_1$, $\tilde{k}_2$	parameters in the expression for $\boldsymbol{k}$ on page 368 $[\mathrm{m}^2]$
$k_{T\sigma}$	thermal diffusion ratio of component σ $[-]$
M	mean molar mass $[\mathrm{kg}\cdot\mathrm{mol}^{-1}]$
M_0	parameter in Section 4 $[\mathrm{kg}\cdot\mathrm{mol}^{-1}]$
M_σ	molar mass of component σ $[\mathrm{kg}\cdot\mathrm{mol}^{-1}]$
$\boldsymbol{n}$	unit outward normal
N^α, $\tilde{N}^\alpha$	numbers of all α nodes in $\overline{\Omega}^{ff}$ and $\overline{\tilde{\Omega}}^{ff}$, respectively
$N_{\mathcal{T}}$	number of triangles in $\mathcal{T}$
N_t	number of time steps in Section 3
N_{ref}	number of nodes in (4.5) and (4.6), page 372
$N_{\mathcal{V}}$	number of finite volumes in $\mathcal{V}$
$\boldsymbol{P}$	pressure tensor [Pa]
p	pressure [Pa]
p_0, p_1, p_2	parameters in Section 4 [Pa]
p_σ	partial pressure of component σ [Pa]

$\boldsymbol{Q}$	heat flow vector $[\mathrm{kg}\cdot\mathrm{s}^{-3}]$
q	heat production per unit volume $[\mathrm{kg}\cdot\mathrm{m}^{-1}\cdot\mathrm{s}^{-3}]$
$q_{f,\mathrm{Neu}}$	flux prescribed on $\Gamma_{f,\mathrm{Neu}}$
R	gas constant $[\mathrm{J}\cdot\mathrm{K}^{-1}\cdot\mathrm{mol}^{-1}]$
ρ_σ	partial density of component σ $[\mathrm{kg}\cdot\mathrm{m}^{-3}]$
$\boldsymbol{S}$	rate-of-shear tensor $[\mathrm{s}^{-1}]$
$\mathcal{T}$	triangulation covering $\overline{\Omega}^{pm}$
$\boldsymbol{t}$	unit vector tangential to $\mathcal{I}$
T	thermodynamic temperature [K]
t	time [s]
T_0	parameter in Section 4 [K]
t_{ini}, t_{fin}	initial and final time, respectively [s]
t_n	n-th time level [s]
$\mathcal{V}$	mesh of finite volumes covering $\overline{\Omega}^{pm}$
$\boldsymbol{v}$	velocity $[\mathrm{m}\cdot\mathrm{s}^{-1}]$
$v_{1,0}$	parameter in Section 4 $[\mathrm{m}\cdot\mathrm{s}^{-1}]$
V_i^α	finite volume associated with $\boldsymbol{x}_i^\alpha$
V_i^e	part of V_i (defined on page 357)
$\boldsymbol{V}_\sigma$	diffusion velocity of component σ $[\mathrm{m}\cdot\mathrm{s}^{-1}]$
$\mathcal{X}$	set of all nodes in $\mathcal{T}$
$\mathcal{X}^\alpha$, $\tilde{\mathcal{X}}^\alpha$	sets of all α nodes in $\overline{\Omega}^{ff}$ and $\overline{\tilde{\Omega}}^{ff}$, respectively
$\boldsymbol{x}_{i,j}^\alpha$	point in $\overline{\tilde{\Omega}}^{ff}$ (defined on page 361)
$\boldsymbol{x}_B^e$	barycenter of triangle T^e (defined on page 357)
$\boldsymbol{x}_e$	circumcenter of triangle T^e (defined on page 357)
$\boldsymbol{x}_i$	node in $\mathcal{T}$
x_i	i-th spatial coordinate [m]
$\boldsymbol{x}_{i,j}$	point in $\overline{\Omega^{pm}}$ (defined on page 357)
$\boldsymbol{x}_{i,j}^b$	point on $\partial\Omega^{pm}$ (defined on page 357)
$\boldsymbol{x}_{i,j}^e$	point in Ω^{pm} (defined on page 357)
$X_{n,0}$, $X_{n,1}$	parameters in Section 4 $[-]$
X_σ	mass fraction of component σ $[-]$
z_{fine}	numerical solution on a very fine mesh (introduced on page 372)
z_h	numerical solution corresponding to h (introduced on page 372)

Subscripts

g	gas
m	combination of properties of the solid matrix and the fluid
n	NAPL vapor
s	solid matrix

Superscripts

1	1-node
2	2-node
ff	free flow
pm	porous medium
s	s-node
T	transpose

Other symbols

$[\boldsymbol{f}]_k, [\boldsymbol{f}]_{k,l}$	components k and k,l of vector and matrix $\boldsymbol{f}$, respectively
$\lvert\Gamma\rvert$	length of line segment Γ
$\lvert V\rvert$	area of V
$\otimes$	tensor product
$\lVert\cdot\rVert$	Euclidean norm
$\lVert\cdot\rVert_\theta$	norm, where $\theta \in \{t, l_1, l_2, \tilde{l_2}\}$ (defined by (4.4)–(4.6) and (4.8), pages 372 and 381)

1 Introduction

A detailed description of compositional flow in a porous medium and in the atmospheric boundary layer above its surface is required in many research areas and applications, including, for example, environmental protection, search for new energy resources or study of climate change (e.g., [8] and [14]). In past years and decades, many researchers have focused on the development and analysis of variously detailed mathematical models of such flow and on the development of numerical models based on these mathematical formulations. The subject of our research is the modeling of NAPL (volatile organic waste chemicals that are in the form of non-aqueous phase liquid) vapor transport (e.g., [29] and [26]) driven by air flow inside a porous medium and above its surface, where this flow is the non-isothermal, compressible flow of a mixture of two gases subject to gravity.

Surprisingly, it seems that no models of such flow are reported in the literature. One can find many models of isothermal single-phase single-component flow (e.g., [2], [5], [11]), where some of them describe only steady flows ([2], [5]). There are also, for example, models of isothermal two phase-flow (e.g., [7], [19]) and non-isothermal models of two-phase two-component flow in the porous medium and single-phase two-component

flow above its surface (e.g., [8], [13], [1], [20]). But to the best of our knowledge, none of existing models that couple flow inside a porous medium and above its surface are capable of modeling non-isothermal compressible flow. Moreover, the model of the interaction among the species in the same phase in the mixture is highly simplified in these models, and the gravitational effects are often neglected (e.g., [13], [1] and [20]). Therefore, the primary aim of this paper is to contribute to the present knowledge and to propose a mathematical formulation and a reliable numerical model for the above mentioned compositional flow.

This paper is structured as follows: In Section 2, we describe our mathematical model and in Section 3, we present our numerical model. In Section 4, we present our numerical results.

2 Mathematical model of coupled flows

Our model is based on the two domain approach (e.g., [2], [5], [11], [7], [19], [13], [1], [20], [28]), i.e., the computational domain is divided into the free flow subdomain and porous medium subdomain. In each subdomain, the flow is described by corresponding conservation laws for mass, momentum and energy. At the interface between these two subdomains, coupling conditions are prescribed allowing the exchange of mass, momentum and energy between the flows (see Fig. 1). This approach allows us to decompose the whole problem into two subproblems which can be solved separately (by using, e.g., different forms of conservation laws and a different numerical scheme in each subdomain), which is very convenient because the phase velocities in a porous medium are much lower than in the free space above its surface.

We assume that the gaseous mixture flowing in the porous medium and in the free space above its surface consists of two components. For simplicity, the first component will be referred to as gas and the second one as NAPL vapor. In each subdomain, the flow of this mixture is described by conservation laws for the mass of the mixture, mass of the NAPL vapor, momentum of the mixture and energy of the mixture.

The conservation laws for the individual flows can be found in the literature on the kinetic theory of gases (e.g., [6], [12] and [16]) and in the publications on transport in

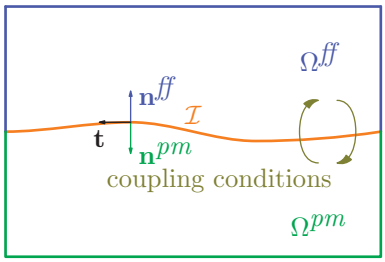

Figure 1: Free flow region Ω^{ff}, porous medium Ω^{pm} and interface $\mathcal{I}$.

porous media (e.g., [21] and [18]). The numerical scheme for the flow inside the porous medium has been already published by the authors [24]. The numerical model for the flow inside the free flow region has been already tested by the authors as well [23]. The types of coupling conditions employed are commonly used (e.g., [11], [13], [1], [20] or [21]).

In the following, the objects related to the porous medium and free flow region are denoted by the superscripts *pm* and *ff*, respectively, when these need to be distinguished. The entire domain $\Omega\subset\mathbb{R}^2$ in which the flow occurs consists of two subdomains Ω^{pm} and Ω^{ff} and of the interface $\mathcal{I}$ between the domains, i.e., $\Omega=\Omega^{pm}\cup\mathcal{I}\cup\Omega^{ff}$ (see Fig. 1). Vectors and matrices are printed in the bold font, and their components are in the non-bold font, i.e., $\boldsymbol{v}=(v_1,v_2)^{\mathrm{T}}$, where T denotes the transpose. The Cartesian spatial coordinates of a point $\boldsymbol{x}\in\Omega$ are denoted by x_i, $i=1,2$. The quantities related to the NAPL vapor and gas are denoted by the subscripts n and g, respectively.

In this text, all of the physical quantities have the units listed in the section Nomenclature. The flow is considered on a time interval $[t_{\mathrm{ini}},t_{\mathrm{fin}}]$.

Although our model is spatially two-dimensional, it can be readily extended to the three-dimensional case (see, e.g., [2], [7], [28]).

2.1 Mathematical model for compressible flow in porous medium

The mathematical model for the flow inside the porous medium reads

$$\phi(\partial\rho/\partial t)+\nabla\cdot(\rho\boldsymbol{v})=F, \tag{2.1}$$

$$\phi(\partial(X_n\rho)/\partial t)+\nabla\cdot(X_n\rho\boldsymbol{v}-D\rho\nabla X_n)=F_n, \tag{2.2}$$

$$\boldsymbol{v}=-(1/\mu)\boldsymbol{k}(\nabla p-\rho\boldsymbol{g}), \tag{2.3}$$

$$\begin{aligned}(\rho c_p)_m(\partial T/\partial t)+\nabla\cdot\left(\rho c_p T\boldsymbol{v}-\lambda_m\nabla T\right)&=\nabla\cdot\left(\rho c_p\boldsymbol{v}\right)T\\ &+q_m+\phi((\partial p/\partial t)+\nabla p\cdot\boldsymbol{v}),\end{aligned} \tag{2.4}$$

where the diffusion coefficient D is defined by

$$D=\phi D_n+a\|\boldsymbol{v}\|. \tag{2.5}$$

The mass fraction X_σ ($\sigma=n,g$) is defined as $X_\sigma=\rho_\sigma/\rho$, where the partial densities satisfy $\rho_n+\rho_g=\rho$. Consequently, we have $X_n+X_g=1$. The specific heat c_p is defined as

$$c_p=c_{p,n}X_n+c_{p,g}X_g, \tag{2.6}$$

and the subscript m in (2.4) denotes the following combinations of the properties of the solid matrix (subscript s) and fluid:

$$\begin{aligned}(\rho c_p)_m&=(1-\phi)(\rho_s c_s)+\phi\rho c_p,\\ \lambda_m&=(1-\phi)\lambda_s+\phi\lambda,\\ q_m&=(1-\phi)q_s+\phi q.\end{aligned} \tag{2.7}$$

The pressure, densities and temperature of the mixture are assumed to be related by the equation of state for the mixture of two ideal gases

$$\rho = pM/(RT), \tag{2.8}$$

where M represents the mean molar mass defined by

$$M = \left(X_n/M_n + X_g/M_g\right)^{-1}. \tag{2.9}$$

For the solution of the system (2.1)–(2.9), the primary variables are p, X_n and T. This system is solved in the following nonconservative form (see [24]):

$$\phi\left(\frac{\partial\rho}{\partial p}\frac{\partial p}{\partial t} + \frac{\partial\rho}{\partial X_n}\frac{\partial X_n}{\partial t} + \frac{\partial\rho}{\partial T}\frac{\partial T}{\partial t}\right) + \nabla\cdot(\rho\boldsymbol{v}) = F, \tag{2.10}$$

$$\phi\rho\frac{\partial X_n}{\partial t} + \phi X_n\left(\frac{\partial\rho}{\partial p}\frac{\partial p}{\partial t} + \frac{\partial\rho}{\partial X_n}\frac{\partial X_n}{\partial t} + \frac{\partial\rho}{\partial T}\frac{\partial T}{\partial t}\right) + \nabla\cdot(X_n\rho\boldsymbol{v} - D\rho\nabla X_n) = F_n, \tag{2.11}$$

$$\begin{aligned}&\left((\rho c_p)_m + \phi c_p T\frac{\partial\rho}{\partial T}\right)\frac{\partial T}{\partial t} + \phi c_p T\frac{\partial\rho}{\partial X_n}\frac{\partial X_n}{\partial t} + \phi\left(c_p T\frac{\partial\rho}{\partial p} - 1\right)\frac{\partial p}{\partial t}\\ &\quad + \nabla\cdot\left(\rho c_p T\boldsymbol{v} - \lambda_m\nabla T\right) = \rho T\nabla c_p\cdot v + q_m + \phi\nabla p\cdot\boldsymbol{v} + Fc_pT,\end{aligned} \tag{2.12}$$

where Eq. (2.12) was obtained by adding the c_pT multiple of (2.1) to (2.4).

The initial conditions are

$$p(t_{\text{ini}},\boldsymbol{x}) = p_{\text{ini}}(\boldsymbol{x}), \quad X_n(t_{\text{ini}},\boldsymbol{x}) = X_{n,\text{ini}}(\boldsymbol{x}), \quad T(t_{\text{ini}},\boldsymbol{x}) = T_{\text{ini}}(\boldsymbol{x}) \quad \forall\boldsymbol{x}\in\overline{\Omega}^{pm}. \tag{2.13}$$

On $\partial\Omega^{pm}$, the following boundary conditions can be prescribed:

$$p = p_{p,\text{Dir}} \quad \text{on} \quad \Gamma_{p,\text{Dir}}, \quad (\rho\boldsymbol{v})\cdot\boldsymbol{n} = q_{p,\text{Neu}} \quad \text{on} \quad \Gamma_{p,\text{Neu}}, \tag{2.14}$$

$$X_n = X_{nX_n,\text{Dir}} \quad \text{on} \quad \Gamma_{X_n,\text{Dir}}, \quad \nabla X_n\cdot\boldsymbol{n} = 0 \quad \text{on} \quad \Gamma_{X_n,\text{out}}, \tag{2.15}$$

$$(X_n\rho\boldsymbol{v} - D\rho\nabla X_n)\cdot\boldsymbol{n} = q_{X_n,\text{Neu}} \quad \text{on} \quad \Gamma_{X_n,\text{Neu}}, \tag{2.16}$$

$$T = T_{T,\text{Dir}} \quad \text{on} \quad \Gamma_{T,\text{Dir}}, \quad \nabla T\cdot\boldsymbol{n} = 0 \quad \text{on} \quad \Gamma_{T,\text{out}}, \tag{2.17}$$

$$\left(\rho c_p T\boldsymbol{v} - \lambda_m\nabla T\right)\cdot\boldsymbol{n} = q_{T,\text{Neu}} \quad \text{on} \quad \Gamma_{T,\text{Neu}}, \tag{2.18}$$

where $\Gamma_{p,\text{Dir}}\cup\Gamma_{p,\text{Neu}} = \partial\Omega^{pm}$ and $\Gamma_{p,\text{Dir}}\cap\Gamma_{p,\text{Neu}} = \emptyset$; $\Gamma_{X_n,\text{Dir}}\cup\Gamma_{X_n,\text{Neu}}\cup\Gamma_{X_n,\text{out}} = \partial\Omega^{pm}$, and $\Gamma_{X_n,\text{Dir}}$, $\Gamma_{X_n,\text{Neu}}$ and $\Gamma_{X_n,\text{out}}$ are pairwise disjoint; $\Gamma_{T,\text{Dir}}\cup\Gamma_{T,\text{Neu}}\cup\Gamma_{T,\text{out}} = \partial\Omega^{pm}$, and $\Gamma_{T,\text{Dir}}$, $\Gamma_{T,\text{Neu}}$ and $\Gamma_{T,\text{out}}$ are pairwise disjoint. The symbol $\boldsymbol{n}$ stands for the unit outward normal to $\partial\Omega^{pm}$.

2.2 Mathematical model for compressible flow in free flow region

The mathematical model for the free flow above the surface of the porous medium reads

$$\partial\rho/\partial t+\nabla\cdot(\rho\boldsymbol{v})=0, \tag{2.19}$$
$$\partial\rho_n/\partial t+\nabla\cdot(\rho_n(\boldsymbol{v}+\boldsymbol{V}_n))=0, \tag{2.20}$$
$$\partial(\rho\boldsymbol{v})/\partial t+\nabla\cdot(\boldsymbol{P}+\rho\boldsymbol{v}\otimes\boldsymbol{v})=\rho\boldsymbol{g}, \tag{2.21}$$
$$\partial(\rho e)/\partial t+\nabla\cdot(\boldsymbol{Q}+\rho e\boldsymbol{v}+\boldsymbol{P}\boldsymbol{v})=\rho\boldsymbol{g}\cdot\boldsymbol{v}, \tag{2.22}$$

where the terms $\boldsymbol{V}_\sigma$, $\boldsymbol{P}$ and $\boldsymbol{Q}$ are defined as

$$\boldsymbol{V}_\sigma=-\textstyle\sum_{\gamma\in\{n,g\}}D_{\sigma,\gamma}(\boldsymbol{d}_\gamma+k_{T\gamma}(\nabla T/T)),\quad \sigma=g,n, \tag{2.23}$$
$$\boldsymbol{P}=p\boldsymbol{I}-2\mu\boldsymbol{S}, \tag{2.24}$$
$$\boldsymbol{Q}=-\lambda\nabla T+p\textstyle\sum_{\sigma\in\{n,g\}}\left(k_{T\sigma}+\frac{\kappa}{\kappa-1}\frac{p_\sigma}{p}\right)\boldsymbol{V}_\sigma. \tag{2.25}$$

Here, the diffusion driving forces $\boldsymbol{d}_\sigma$ and rate-of-shear tensor $\boldsymbol{S}$ are defined as

$$\boldsymbol{d}_\sigma=\nabla(p_\sigma/p)+(p_\sigma/p-\rho_\sigma/\rho)(\nabla p/p),\quad \sigma=g,n, \tag{2.26}$$
$$\boldsymbol{S}_{i,j}=(1/2)\left(\partial v_j/\partial x_i+\partial v_i/\partial x_j\right)-(1/3)\nabla\cdot\boldsymbol{v}\delta_{i,j},\quad i,j=1,2. \tag{2.27}$$

The partial pressures p_σ and thermal diffusion ratios $k_{T\sigma}$ satisfy $p_n+p_g=p$ and $k_{Tn}=-k_{Tg}$. The multicomponent diffusion coefficients $D_{\sigma,\gamma}$, where $\sigma,\gamma=g,n$, fulfill the conditions

$$\begin{aligned}&D_{\sigma,\gamma}=D_{\gamma,\sigma}\quad\text{for}\quad\sigma\neq\gamma,\\&D_{\sigma,\sigma}=-(\rho_\gamma/\rho_\sigma)D_{\gamma,\sigma}\quad\text{for}\quad\sigma\neq\gamma,\quad\rho_\sigma\neq0.\end{aligned} \tag{2.28}$$

(When $\rho_\sigma=0$, $D_{\sigma,\sigma}$ is not needed.) The ratio of specific heats κ is defined by $\kappa=c_p/c_V$, where c_p is given by (2.6), and c_V is defined as

$$c_V=c_{V,n}X_n+c_{V,g}X_g. \tag{2.29}$$

The above system of equations is supplemented by the formula

$$\rho e=c_V\rho T+\rho\boldsymbol{v}^2/2. \tag{2.30}$$

Combining (2.8) and (2.30) with the Mayer relation $M(c_p-c_V)=R$, we get the following expression relating the energy to the pressure

$$p=(\kappa-1)\left(\rho e-\rho\boldsymbol{v}^2/2\right). \tag{2.31}$$

Note that for $\rho_n=0$, the above system reduces to the compressible Navier-Stokes equations and the corresponding energy balance equation.

In system (2.8) and (2.19)–(2.31), the primary variables are ρ, ρ_n, ρv_1, ρv_2 and ρe. The initial conditions are

$$\rho(t_{\text{ini}},\boldsymbol{x})=\rho_{\text{ini}}(\boldsymbol{x}),\quad \rho_n(t_{\text{ini}},\boldsymbol{x})=\rho_{n,\text{ini}}(\boldsymbol{x}), \tag{2.32}$$
$$T(t_{\text{ini}},\boldsymbol{x})=T_{\text{ini}}(\boldsymbol{x}),\quad \boldsymbol{v}(t_{\text{ini}},\boldsymbol{x})=\boldsymbol{v}_{\text{ini}}(\boldsymbol{x}) \tag{2.33}$$

$\forall\boldsymbol{x}\in\overline{\Omega}^{ff}$. The boundary conditions will be described in Section 4.

2.3 Coupling conditions

In this section, we discuss the coupling conditions prescribed at the interface $\mathcal{I}$ which couple the free flow and porous medium flow presented in previous sections. These conditions were explored, for example, for non-isothermal incompressible compositional flow in [8], [13], [1] and [20] and for isothermal incompressible single-phase single-component flow in [11] and [21].

We use the following coupling conditions (see Fig. 1, page 351):

- Conditions at the interface $\mathcal{I}$ for the porous medium flow in Ω^{pm}:
  - For the pressure p in Eq. (2.10):
$$p^{pm} := [((\boldsymbol{P}+\rho \boldsymbol{v}\otimes\boldsymbol{v})\boldsymbol{n})\cdot\boldsymbol{n}]^{ff}. \tag{2.34}$$
  - For the mass fraction of the NAPL vapor X_n or, alternatively, for the mass flux of the NAPL vapor in Eq. (2.11):
$$X_n^{pm} := X_n^{ff} \tag{2.35}$$
or
$$[(X_n\rho\boldsymbol{v} - D\rho\nabla X_n)\cdot\boldsymbol{n}]^{pm} := -[(\rho_n(\boldsymbol{v}+\boldsymbol{V}_n))\cdot\boldsymbol{n}]^{ff}. \tag{2.36}$$
  - For the heat flux in Eq. (2.12):
$$\left[\left(\rho c_p T\boldsymbol{v} - \lambda_m\nabla T\right)\cdot\boldsymbol{n}\right]^{pm} := -[(\boldsymbol{Q}+\rho e\boldsymbol{v}+\boldsymbol{P}\boldsymbol{v})\cdot\boldsymbol{n}]^{ff}. \tag{2.37}$$
- Conditions at the interface $\mathcal{I}$ for the free flow in Ω^{ff}:
  - For the mass flux in Eq. (2.19) and for the component x_2 of the momentum $\rho\boldsymbol{v}$ in Eq. (2.21):
$$[\rho\boldsymbol{v}\cdot\boldsymbol{n}]^{ff} := -[\rho\boldsymbol{v}\cdot\boldsymbol{n}]^{pm}. \tag{2.38}$$
  - For the rate-of-shear tensor $\boldsymbol{S}$ in Eq. (2.21):
$$2[\boldsymbol{S}\boldsymbol{n}]^{ff}\cdot\boldsymbol{t} := -\frac{\alpha_{\mathrm{BJ}}}{\sqrt{\boldsymbol{t}^{\mathrm{T}}\boldsymbol{k}\boldsymbol{t}}}\left(\boldsymbol{v}^{ff}-\boldsymbol{v}^{pm}\right)\cdot\boldsymbol{t}. \tag{2.39}$$
    Note that Eq. (2.39) is the condition listed in [20]. But in our case, the velocity of the porous medium flow is not neglected (similarly as in [11] and [21]).
  - For the mass fraction of the NAPL vapor X_n or, alternatively, for the flux of the NAPL vapor in Eq. (2.20):
$$X_n^{ff} := X_n^{pm} \tag{2.40}$$
or
$$[(\rho_n(\boldsymbol{v}+\boldsymbol{V}_n))\cdot\boldsymbol{n}]^{ff} := -[(X_n\rho\boldsymbol{v} - D\rho\nabla X_n)\cdot\boldsymbol{n}]^{pm}. \tag{2.41}$$

– For the temperature T in Eq. (2.22):

$$T^{ff} := T^{pm}. \tag{2.42}$$

When employing the above conditions, the quantities on the left-hand sides are determined by the corresponding quantities on the right-hand sides. For Eqs. (2.11) and (2.20), we use either (2.35) together with (2.41) or (2.36) together with (2.40).

3 Numerical solution

The complete system of equations is solved by two numerical schemes used by the authors in their past work ([24] and [23]). These two schemes are coupled via discretized versions of the coupling conditions from Section 2.3. In the following sections, the individual parts of the resulting numerical model are described.

3.1 Numerical scheme for compressible flow in porous medium

The spatial discretization of the governing equations is carried out via the control volume based finite element method (e.g., [15] and [25]). The reasons for employing this method are its simplicity and suitability for handling heterogeneous porous media.

Using this method, the domain Ω^{pm} is covered by a boundary conforming Delaunay triangulation $\mathcal{T} = \{T^e\}_{e=1}^{N_\mathcal{T}}$ [30]. All functions involved are approximated using the linear Lagrange finite elements, where each node $\boldsymbol{x}_i$ of $\mathcal{T}$ is associated with the basis function φ_i. Further, Ω^{pm} is also covered by a node-centered dual mesh of finite volumes $\mathcal{V} = \{V_i\}_{i=1}^{N_\mathcal{V}}$ based on the Voronoi diagrams [30]. The time interval $[t_{\text{ini}}, t_{\text{fin}}]$ is divided by means of a strictly increasing sequence $(t_n)_{n=0}^{N_t}$, where $t_0 = t_{\text{ini}}$, $t_{N_t} = t_{\text{fin}}$ and $t_n = t_{\text{ini}} + n\tau$ for a time step τ.

For the description of the numerical scheme, we shall use the following notation (see Fig. 2):

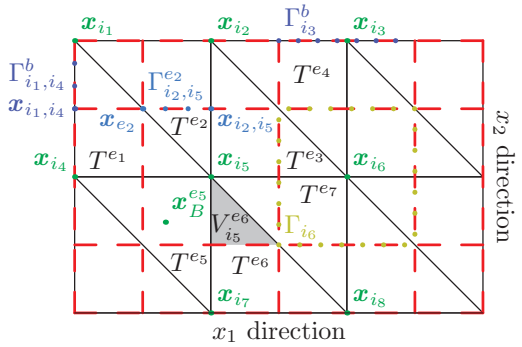

Figure 2: Triangulation (solid line) and mesh of finite volumes (dashed line). According to the notation introduced in Section 3.1, we have $\Lambda^{e_1} = \{i_1, i_4, i_5\}$, $\Lambda_{i_5} = \{i_1, i_2, i_4, i_6, i_7, i_8\}$, $\Lambda^{e_2}_{i_5} = \{i_1, i_2\}$, $\Lambda^b_{i_2} = \{i_1, i_3\}$, $\Lambda_{i_2,i_5} = \{e_2, e_3\}$ and $\Lambda^n_{i_2} = \{e_2, e_3, e_4\}$. The gray region is $V^{e_6}_{i_5}$. The dotted lines are $\Gamma^b_{i_1,i_4}$, $\Gamma^{e_2}_{i_2,i_5}$, $\Gamma^b_{i_3}$ and Γ_{i_6}.

- $\mathcal{X}=\{\boldsymbol{x}_i\}_{i=1}^{N_\mathcal{V}}$ is the set of all nodes in the triangulation $\mathcal{T}$;
- $\Lambda^e=\{i|\boldsymbol{x}_i\in T^e\}$ for a triangle $T^e\in\mathcal{T}$;
- $\Lambda_i=\{j|(\exists T^e\in\mathcal{T})(i\in\Lambda^e\wedge j\in\Lambda^e)\}\setminus\{i\}$;
- $\Lambda_i^e=\Lambda^e\cap\Lambda_i$;
- $\Lambda_i^b=\Lambda_i\cap\{j|\boldsymbol{x}_j\in\partial\Omega^{pm}\}$;
- $\Lambda_{i,j}=\{e|i\in\Lambda^e\wedge j\in\Lambda^e\}$;
- $\Lambda_i^n=\{e|i\in\Lambda^e\}$;
- $\boldsymbol{x}_{i,j}$ is the midpoint of the line segment connecting the nodes $\boldsymbol{x}_i$ and $\boldsymbol{x}_j$;
- $\boldsymbol{x}_e$ is the circumcenter of the triangle T^e;
- $\boldsymbol{x}_B^e$ is the barycenter of the triangle T^e;
- $\Gamma_{i,j}^e$ is the line segment connecting the points $\boldsymbol{x}_e$ and $\boldsymbol{x}_{i,j}$ for $\boldsymbol{x}_e\neq\boldsymbol{x}_{i,j}$;
- $\Gamma_{i,j}^b$ is the line segment connecting the boundary points $\boldsymbol{x}_i$ and $\boldsymbol{x}_{i,j}$;
- $\Gamma_i=\bigcup_{j\in\Lambda_i}\bigcup_{e\in\Lambda_{i,j}}\Gamma_{i,j}^e$;
- $\Gamma_i^b=\bigcup_{j\in\Lambda_i^b}\Gamma_{i,j}^b$ for $\boldsymbol{x}_i\in\partial\Omega^{pm}$;
- $\boldsymbol{x}_{i,j}^e$ and $\boldsymbol{x}_{i,j}^b$ are the midpoints of $\Gamma_{i,j}^e$ and $\Gamma_{i,j}^b$, respectively;
- $\Lambda_{f,\mathrm{Neu},i}^b=\left\{j\in\Lambda_i^b|\boldsymbol{x}_{i,j}^b\in\Gamma_{f,\mathrm{Neu}}\right\}$, where $f=p,X_n,T$;
- $\Lambda_{X_n,\mathrm{out},i}^b=\left\{j\in\Lambda_i^b|\boldsymbol{x}_{i,j}^b\in\Gamma_{X_n,\mathrm{out}}\right\}$;
- $V_i^e=V_i\cap T^e$;
- $f(\boldsymbol{x}_i)=f_i$, $f(\boldsymbol{x}_{i,j})=f_{i,j}$, $f(\boldsymbol{x}_{i,j}^e)=f_{i,j}^e$, $f(\boldsymbol{x}_{i,j}^b)=f_{i,j}^b$ and $f(\boldsymbol{x}_B^e)=f_B^e$, where the time coordinate is omitted;
- f_e is the constant value of f on $T^e\in\mathcal{T}$;
- $f(t_n)=f^n$, where $f=f(t)$.

Using the notation given above, the finite volume V_i is the open set surrounded by the curve Γ_i (i.e., $\partial V_i=\Gamma_i$) for $\boldsymbol{x}_i\notin\partial\Omega^{pm}$ and by the curve $\Gamma_i\cup\Gamma_i^b$ (i.e., $\partial V_i=\Gamma_i\cup\Gamma_i^b$) for $\boldsymbol{x}_i\in\partial\Omega^{pm}$. An example of a mesh of such finite volumes is depicted in Fig. 2.

The numerical scheme is derived (see [24]) by integrating (2.10)–(2.12) over a volume V_i, using the Green formula, approximating all the functions and integrals, approximating the time derivatives by backward finite differences, subtracting the $c_{p,i}^{n+1}T_i^{n+1}$ multiple of the equation resulting from (2.10) from the equation resulting from (2.12) and replacing some values from the new time level by the values from the previous one.

In this procedure, the parameters $\boldsymbol{k}$, ϕ, c_s, ρ_s and λ_s are approximated by constant values $\boldsymbol{k}_e$, ϕ_e, $c_{s,e}$, $\rho_{s,e}$ and $\lambda_{s,e}$ on each triangle $T^e\in\mathcal{T}$, and the parameters μ, λ, $c_{p,n}$ and $c_{p,g}$ are positive constants. Similarly, $\boldsymbol{g}$ is constant. The integrals arising in the derivation of the scheme are approximated in the following way (the time coordinate is omitted):

- $\int_{V_i} f(\boldsymbol{x})g(\boldsymbol{x})\,\mathrm{d}\boldsymbol{x}\approx\sum_{e\in\Lambda_i^n}\left|V_i^e\right|f_ig_e$, where g is constant on each $T^e\in\mathcal{T}$;
- $\int_{V_i}\boldsymbol{f}(\boldsymbol{x})\cdot\boldsymbol{h}(\boldsymbol{x})\,\mathrm{d}\boldsymbol{x}\approx\sum_{e\in\Lambda_i^n}\left|V_i^e\right|\boldsymbol{f}_B^e\cdot\boldsymbol{h}_B^e$;
- $\int_{\Gamma_i}\boldsymbol{f}(s)\cdot\boldsymbol{n}\,\mathrm{d}s\approx\sum_{j\in\Lambda_i}\sum_{e\in\Lambda_{i,j}^e}\left|\Gamma_{i,j}^e\right|\boldsymbol{f}_{i,j}^e\cdot\boldsymbol{n}_{i,j}^e$, where $\boldsymbol{n}_{i,j}^e$ is the unit outward normal with respect to $\Gamma_{i,j}^e$;
- $\int_{\Gamma_i^b}\boldsymbol{f}(s)\cdot\boldsymbol{n}\,\mathrm{d}s\approx\sum_{j\in\Lambda_i^b}\left|\Gamma_{i,j}^b\right|\boldsymbol{f}_{i,j}^b\cdot\boldsymbol{n}_{i,j}^b$, where $\boldsymbol{n}_{i,j}^b$ denotes the unit outward normal with respect to $\Gamma_{i,j}^b$.

Using the aforementioned procedure and considering boundary conditions (2.14)–(2.18), we get the following system of linear algebraic equations for the unknown values p_i^{n+1}, $X_{n,i}^{n+1}$ and T_i^{n+1}, where $n=0,1,\cdots,N_t-1$:

$$\begin{aligned}&\sum_{e\in\Lambda_i^n}|V_i^e|\phi_e\left(\frac{\partial\rho}{\partial p}\right)_i^n\frac{p_i^{n+1}-p_i^n}{\tau}+\sum_{e\in\Lambda_i^n}|V_i^e|\phi_e\left(\frac{\partial\rho}{\partial X_n}\right)_i^n\frac{X_{n,i}^{n+1}-X_{n,i}^n}{\tau}\\&\quad+\sum_{e\in\Lambda_i^n}|V_i^e|\phi_e\left(\frac{\partial\rho}{\partial T}\right)_i^n\frac{T_i^{n+1}-T_i^n}{\tau}+\sum_{j\in\Lambda_i}\sum_{e\in\Lambda_{i,j}}\left|\Gamma_{i,j}^e\right|\rho_{i,j}^{e,n}\boldsymbol{v}_{i,j}^{e,n+1}\cdot\boldsymbol{n}_{i,j}^e\\&\quad+\sum_{j\in\Lambda_{p,\mathrm{Neu},i}^b}\left|\Gamma_{i,j}^b\right|q_{p,\mathrm{Neu},i,j}^{b,n+1}=\sum_{e\in\Lambda_i^n}|V_i^e|F_i^{n+1}\end{aligned}\tag{3.1}$$

for $i=1,2,\cdots,N_{\mathcal{V}}$, $\boldsymbol{x}_i\notin\Gamma_{p,\mathrm{Dir}}$,

$$p_i^{n+1}=p_{p,\mathrm{Dir},i}^{n+1}\quad\text{for } i=1,2,\cdots,N_{\mathcal{V}},\quad\boldsymbol{x}_i\in\Gamma_{p,\mathrm{Dir}},\tag{3.2}$$

$$\begin{aligned}&\sum_{e\in\Lambda_i^n}|V_i^e|\phi_e\rho_i^n\frac{X_{n,i}^{n+1}-X_{n,i}^n}{\tau}+\sum_{e\in\Lambda_i^n}|V_i^e|\phi_eX_{n,i}^n\left(\frac{\partial\rho}{\partial p}\right)_i^n\frac{p_i^{n+1}-p_i^n}{\tau}\\&\quad+\sum_{e\in\Lambda_i^n}|V_i^e|\phi_eX_{n,i}^n\left(\frac{\partial\rho}{\partial X_n}\right)_i^n\frac{X_{n,i}^{n+1}-X_{n,i}^n}{\tau}+\sum_{e\in\Lambda_i^n}|V_i^e|\phi_eX_{n,i}^n\left(\frac{\partial\rho}{\partial T}\right)_i^n\frac{T_i^{n+1}-T_i^n}{\tau}\end{aligned}$$

$$+\sum_{j\in\Lambda_i}\sum_{e\in\Lambda_{i,j}}\left|\Gamma^e_{i,j}\right|\rho^{e,n}_{i,j}\boldsymbol{n}^e_{i,j}\cdot\left(\underline{X^{e,n+1}_{n,i,j}}\boldsymbol{v}^{e,n}_{i,j}-D^{e,n}_{i,j}\nabla X^{e,n+1}_{n,i,j}\right)$$
$$+\sum_{j\in\Lambda^b_{X_n,\mathrm{out},i}}\left|\Gamma^b_{i,j}\right|X^{n+1}_{n,i}q^{b,n+1}_{p,\mathrm{Neu},i,j}+\sum_{j\in\Lambda^b_{X_n,\mathrm{Neu},i}}\left|\Gamma^b_{i,j}\right|q^{b,n+1}_{X_n,\mathrm{Neu},i,j}=\sum_{e\in\Lambda^n_i}|V^e_i|F^{n+1}_{n,i} \tag{3.3}$$

for $i=1,2,\cdots,N_{\mathcal{V}}$, $\boldsymbol{x}_i\notin\Gamma_{X_n,\mathrm{Dir}}$,

$$X^{n+1}_{n,i}=X^{n+1}_{n,X_n,\mathrm{Dir},i}\quad\text{for } i=1,2,\cdots,N_{\mathcal{V}},\quad \boldsymbol{x}_i\in\Gamma_{X_n,\mathrm{Dir}}, \tag{3.4}$$

$$\sum_{e\in\Lambda^n_i}|V^e_i|\left(\phi_e\rho^n_i c^n_{p,i}+(1-\phi_e)\rho_{s,e}c_{s,e}\right)\frac{T^{n+1}_i-T^n_i}{\tau}-\sum_{e\in\Lambda^n_i}|V^e_i|\phi_e\frac{p^{n+1}_i-p^n_i}{\tau}$$
$$+\sum_{j\in\Lambda_i}\sum_{e\in\Lambda_{i,j}}\left|\Gamma^e_{i,j}\right|\left(\rho^{e,n}_{i,j}c^{e,n}_{p,i,j}\underline{T^{e,n+1}_{i,j}}\boldsymbol{v}^{e,n}_{i,j}-\lambda^e_{m,i,j}\nabla T^{e,n+1}_{i,j}\right)\cdot\boldsymbol{n}^e_{i,j}$$
$$+\sum_{j\in\Lambda^b_{T,\mathrm{Neu},i}}\left|\Gamma^b_{i,j}\right|q^{b,n+1}_{T,\mathrm{Neu},i,j}-\sum_{j\in\Lambda^b_{T,\mathrm{Neu},i}}\left|\Gamma^b_{i,j}\right|c^n_{p,i}T^{n+1}_i q^{b,n+1}_{p,\mathrm{Neu},i,j}$$
$$-\sum_{j\in\Lambda_i}\sum_{e\in\Lambda_{i,j}}\left|\Gamma^e_{i,j}\right|\left(\rho^{e,n}_{i,j}c^{e,n}_{p,i,j}T^{e,n+1}_{i,j}\boldsymbol{v}^{e,n}_{i,j}\right)\cdot\boldsymbol{n}^e_{i,j}$$
$$=\sum_{e\in\Lambda^n_i}|V^e_i|q^{n+1}_{m,i}+\sum_{e\in\Lambda^n_i}|V^e_i|\left(\phi_e\nabla p^{e,n+1}_B+\rho^{e,n}_B T^{e,n+1}_B\nabla c^{e,n}_{p,B}\right)\cdot\boldsymbol{v}^{e,n}_B \tag{3.5}$$

for $i=1,2,\cdots,N_{\mathcal{V}}$, $\boldsymbol{x}_i\notin\Gamma_{T,\mathrm{Dir}}$,

$$T^{n+1}_i=T^{n+1}_{T,\mathrm{Dir},i}\quad\text{for}\quad i=1,2,\cdots,N_{\mathcal{V}},\quad \boldsymbol{x}_i\in\Gamma_{T,\mathrm{Dir}}. \tag{3.6}$$

In these equations, the underlined terms are calculated using the full upwind formula

$$\underline{f^{e,n+1}_{i,j}}=\begin{cases}f^{n+1}_i, & \boldsymbol{v}^{e,n}_{i,j}\cdot\boldsymbol{n}^e_{i,j}\geq 0,\\ f^{n+1}_j, & \boldsymbol{v}^{e,n}_{i,j}\cdot\boldsymbol{n}^e_{i,j}<0,\end{cases} \tag{3.7}$$

and the term $\boldsymbol{v}^{e,n+1}_{i,j}$ is approximated as

$$\boldsymbol{v}^{e,n+1}_{i,j}\approx-(1/\mu)\boldsymbol{k}_e\left(\nabla p^{e,n+1}_B-p^{e,n+1}_{i,j}(\partial\rho/\partial p)^{e,n}_{i,j}\boldsymbol{g}\right). \tag{3.8}$$

Note that in the course of the derivation of Eq. (3.5), the boundary integrals over $\Gamma_{T,\mathrm{out}}$ canceled out.

Eqs. (3.1)–(3.6) are subject to the initial conditions

$$p^0_i=p_{\mathrm{ini},i},\quad X^0_{n,i}=X_{n,\mathrm{ini},i},\quad T^0_i=T_{\mathrm{ini},i}\quad\text{for } i=1,2,\cdots,N_{\mathcal{V}}. \tag{3.9}$$

Since linear system (3.1)–(3.9) is sparse, it is solved by UMFPACK from the SuiteSparse package [9] via the LU factorization after which an iterative refinement is performed.

3.2 Numerical scheme for compressible flow in free flow region

The system of the governing equations describing the free flow is solved via the method of lines in which the spatial discretization is carried out by the finite volume method with the staggered arrangement of variables [25]. Based on the experience of the authors, this scheme proves to be more stable than the control volume based finite element method for the free flow in the setup considered in this paper. For the time integration, the Runge-Kutta-Merson method with the time step adaptivity [17] is employed, where the adaptivity is crucial because the solver needs to start with a shorter time step after the interface values are updated.

For simplicity, the domain Ω^{ff} is assumed to be rectangular. This domain is covered by an orthogonal mesh as in Fig. 3, i.e., by rectangles. The scalar variables are located at the nodes (referred to as s-nodes) of this mesh, respectively. The components ρv_1 and ρv_2 of the vector $\rho \boldsymbol{v}$ are located at the midpoints (referred to as 1- and 2-nodes) of the horizontal and vertical edges of this mesh, respectively. The s-, 1- and 2-nodes will be denoted by the superscripts s, 1 and 2. Each s-, 1- and 2-node which does not lie on $\partial\Omega^{ff}$ is surrounded by the rectangular finite volume each side of which lies on the axis of symmetry of the line segment connecting this node with a neighboring s-, 1- and 2-node, respectively. For the nodes on $\partial\Omega^{ff}$, the sides of the surrounding finite volume lie on the aforementioned axes of symmetry and on $\partial\Omega^{ff}$ (see the boundary volume V_9^s in Fig. 3).

In our simulations, the mesh covering Ω^{ff} is extended by one layer of auxiliary rectangles [4] at the left and right end of Ω^{ff} (according to Fig. 4, page 366). The boundary conditions on the left and right side of Ω^{ff} are prescribed at the new boundary nodes (referred to as the 'dummy nodes'). The extended domain will be denoted by $\tilde{\Omega}^{ff}$. Describing the spatial discretization in detail, we shall use the following notation, where $\alpha = s,1,2$ (see Fig. 3):

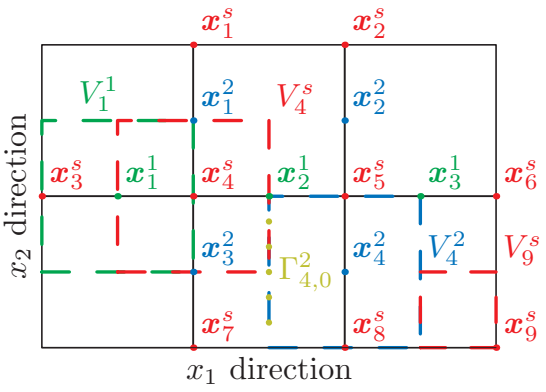

Figure 3: Mesh of rectangles (solid line) and selected finite volumes (dashed line). According to the notation introduced in Section 3.2, we have $\boldsymbol{x}_{4,0}^s = \boldsymbol{x}_1^1$, $\boldsymbol{x}_{4,1}^s = \boldsymbol{x}_3^2$, $\boldsymbol{x}_{4,2}^s = \boldsymbol{x}_2^1$, $\boldsymbol{x}_{4,3}^s = \boldsymbol{x}_1^2$ and so on. The dotted line is $\Gamma_{4,0}^2$.

- $\mathcal{X}^\alpha = \{\boldsymbol{x}_i^\alpha\}_{i=1}^{N^\alpha}$ and $\tilde{\mathcal{X}}^\alpha = \{\boldsymbol{x}_i^\alpha\}_{i=1}^{\tilde{N}^\alpha}$ are the sets of all α-nodes in Ω^{ff} and in $\tilde{\Omega}^{ff}$, respectively.
- V_i^α is the finite volume associated with the node $\boldsymbol{x}_i^\alpha$.
- $\Gamma_{i,j}^\alpha$ is the j-th face of the volume V_i^α, where the faces are numbered counterclockwise from 0 to 3 beginning with the left face (see Fig. 3).
- $\boldsymbol{x}_{i,j}^\alpha$ is the midpoint of $\Gamma_{i,j}^\alpha$.
- $f(\boldsymbol{x}_i^\alpha) = f_i^\alpha$ and $f(\boldsymbol{x}_{i,j}^\alpha) = f_{i,j}^\alpha$, where the time coordinate is omitted.
- $\dot{f}$ is the time derivative of f, where $f = f(t)$.

We remark that the aforementioned notation differs from the notation used in [23]. The following approximations also slightly differ.

The numerical scheme is derived (see [23]) by integrating each of Eqs. (2.19)–(2.22) over a corresponding volume V_i^α, using the Green formula and approximating the integrals according to the following formulas:

- $\int_{V_i^\alpha} f(\boldsymbol{x})\,\mathrm{d}\boldsymbol{x} \approx |V_i^\alpha| f_i^\alpha$;
- $\int_{\partial V_i^\alpha} \boldsymbol{f}(s)\cdot\boldsymbol{n}\,\mathrm{d}s \approx \sum_{j=0}^3 |\Gamma_{i,j}^\alpha| \boldsymbol{f}_{i,j}^\alpha \cdot \boldsymbol{n}_{i,j}^\alpha$, where $\boldsymbol{n}_{i,j}^\alpha$ denotes the unit outward normal with respect to $\Gamma_{i,j}^\alpha$.

For each node $\boldsymbol{x}_i^\alpha$ at which the values of the primary variables are not prescribed as the Dirichlet boundary conditions or calculated via extrapolation, the aforementioned procedure yields

$$|V_i^s|\dot{\rho}_i^s + \sum_{j=0}^3 |\Gamma_{i,j}^s| \underline{\rho_{i,j}^s} \boldsymbol{v}_{i,j}^s \cdot \boldsymbol{n}_{i,j}^s = 0, \tag{3.10}$$

$$|V_i^s|\dot{\rho}_{n,i}^s + \sum_{j=0}^3 |\Gamma_{i,j}^s| \underline{\rho_{n,i,j}^s} \left(\boldsymbol{v}_{i,j}^s + \boldsymbol{V}_{n,i,j}^s\right)\cdot \boldsymbol{n}_{i,j}^s = 0, \tag{3.11}$$

$$|V_i^1|(\rho\dot{v}_1)_i^1 + \sum_{j=0}^3 |\Gamma_{i,j}^1| \left[\boldsymbol{P}_{i,j}^1 \cdot \boldsymbol{n}_{i,j}^1\right]_1 + \sum_{j=0}^3 |\Gamma_{i,j}^1| \underline{(\rho v_1)_{i,j}^1} \boldsymbol{v}_{i,j}^1 \cdot \boldsymbol{n}_{i,j}^1 = |V_i^1|\rho_i^1 g_1, \tag{3.12}$$

$$|V_i^2|(\rho\dot{v}_2)_i^2 + \sum_{j=0}^3 |\Gamma_{i,j}^2| \left[\boldsymbol{P}_{i,j}^2 \cdot \boldsymbol{n}_{i,j}^2\right]_2 + \sum_{j=0}^3 |\Gamma_{i,j}^2| \underline{(\rho v_2)_{i,j}^2} \boldsymbol{v}_{i,j}^2 \cdot \boldsymbol{n}_{i,j}^2 = |V_i^2|\rho_i^2 g_2, \tag{3.13}$$

$$|V_i^s|(\dot{\rho e})_i^s + \sum_{j=0}^3 |\Gamma_{i,j}^s| \left[\boldsymbol{P}_{i,j}^s \cdot \boldsymbol{v}_{i,j}^s + \boldsymbol{Q}_{i,j}^s + \underline{(\rho e)_{i,j}^s} \boldsymbol{v}_{i,j}^s\right]\cdot \boldsymbol{n}_{i,j}^s = |V_i^s| \boldsymbol{g}\cdot(\rho\boldsymbol{v})_i^s, \tag{3.14}$$

where

$$\boldsymbol{V}_{n,i,j}^s = -\sum_{\sigma\in\{n,g\}} D_{n,\sigma,i,j}^s \left(\boldsymbol{d}_{\sigma,i,j}^s + k_{T_\sigma,i,j}^s \left(\nabla T_{i,j}^s / T_{i,j}^s\right)\right), \tag{3.15}$$

$$\boldsymbol{d}_{\sigma,i,j}^s = \nabla(p_\sigma/p)_{i,j}^s + \left(p_{\sigma,i,j}^s/p_{i,j}^s - (\rho_\sigma/\rho)_{i,j}^s\right)\left(\nabla p_{i,j}^s / p_{i,j}^s\right), \tag{3.16}$$

$$\boldsymbol{P}_{i,j}^\alpha = (p\boldsymbol{I} - 2\mu\boldsymbol{S})_{i,j}^\alpha, \tag{3.17}$$

$$\left[\boldsymbol{S}^{\alpha}_{i,j}\right]_{k,l} = (1/2)\left(\partial v_l/\partial x_k + \partial v_k/\partial x_l\right)^{\alpha}_{i,j} - (1/3)\left(\nabla\cdot\boldsymbol{v}\delta_{k,l}\right)^{\alpha}_{i,j}, \tag{3.18}$$

$$\boldsymbol{Q}^{s}_{i,j} = -\lambda(\nabla T)^{s}_{i,j} + p^{s}_{i,j}\sum_{\sigma\in\{n,g\}}\left[k^{s}_{T_\sigma,i,j} + \left(\kappa^{s}_{i,j}/\left(\kappa^{s}_{i,j}-1\right)\right)\left(p^{s}_{\sigma,i,j}/p^{s}_{i,j}\right)\right]\boldsymbol{V}^{s}_{\sigma,i,j} \tag{3.19}$$

for $\alpha = s,1,2$; $k,l = 1,2$ and $\sigma = n,g$.

Similarly as in Section 3.1, the underlined terms are modified by the upwind formula

$$\underline{f^{\alpha}_{i,j}} = \begin{cases} f^{\alpha}_{i}, & \boldsymbol{v}^{\alpha}_{i,j}\cdot\boldsymbol{n}^{\alpha}_{i,j} \geq 0 \quad \text{or} \quad \Gamma^{\alpha}_{i,j} \subset \partial\tilde{\Omega}^{ff}, \\ f^{\alpha}_{k}, & \boldsymbol{v}^{\alpha}_{i,j}\cdot\boldsymbol{n}^{\alpha}_{i,j} < 0 \quad \text{and} \quad \Gamma^{\alpha}_{i,j} \not\subset \partial\tilde{\Omega}^{ff}, \end{cases} \tag{3.20}$$

where $\boldsymbol{x}^{\alpha}_{k}$ is a node different from $\boldsymbol{x}^{\alpha}_{i}$ for which $\partial V^{\alpha}_{i} \cap \partial V^{\alpha}_{k} = \Gamma^{\alpha}_{i,j}$.

If a flux value is prescribed on a face $\Gamma^{\alpha}_{i,j}$ (for example, coupling condition (2.41) is used), the corresponding summand in (3.10)–(3.14) is replaced by the prescribed value.

The values of the functions at the nodes at which they are not located are calculated via the linear interpolation from the nearest function values. Therefore, we have, for example, (see Fig. 3, page 360)

$$\rho^{s}_{4,2} = \rho^{1}_{2} \approx \left(\rho^{s}_{4} + \rho^{s}_{5}\right)/2,$$
$$\left[\boldsymbol{v}^{s}_{4,2}\right]_2 = v_2(\boldsymbol{x}^{s}_{4,2}) = v_2(\boldsymbol{x}^{1}_{2}) \approx \frac{v_{2,u} - v_{2,d}}{\left[\boldsymbol{x}^{2}_{1}\right]_2 - \left[\boldsymbol{x}^{2}_{3}\right]_2}\left(\left[\boldsymbol{x}^{s}_{4}\right]_2 - \left[\boldsymbol{x}^{2}_{3}\right]_2\right) + v_{2,d},$$

where

$$v_{2,u} = \left(v_2(\boldsymbol{x}^{2}_{1}) + v_2(\boldsymbol{x}^{2}_{2})\right)/2, \quad v_{2,d} = \left(v_2(\boldsymbol{x}^{2}_{3}) + v_2(\boldsymbol{x}^{2}_{4})\right)/2.$$

The spatial derivatives are calculated from the nearest function values too. Therefore, we have, e.g.,

$$\frac{\partial v_1}{\partial x_1}(\boldsymbol{x}^{s}_{4,2}) = \frac{\partial v_1}{\partial x_1}(\boldsymbol{x}^{1}_{2}) \approx \frac{v_1(\boldsymbol{x}^{1}_{1}) - v_1(\boldsymbol{x}^{1}_{3})}{\left[\boldsymbol{x}^{1}_{1}\right]_1 - \left[\boldsymbol{x}^{1}_{3}\right]_1},$$
$$\frac{\partial v_2}{\partial x_2}(\boldsymbol{x}^{2}_{4,1}) = \frac{\partial v_2}{\partial x_2}(\boldsymbol{x}^{s}_{8}) \approx \frac{v_2(\boldsymbol{x}^{2}_{2}) - v_2(\boldsymbol{x}^{2}_{4})}{\left[\boldsymbol{x}^{2}_{2}\right]_2 - \left[\boldsymbol{x}^{2}_{4}\right]_2}.$$

System (3.10)–(3.14) is considered together with the following initial conditions:

$$\rho^{s}_{i}(t_{\text{ini}}) = \rho_{\text{ini}}(\boldsymbol{x}^{s}_{i}) \quad \text{for} \quad i = 1,2,\cdots,\tilde{N}^{s}, \tag{3.21}$$
$$\rho^{s}_{n,i}(t_{\text{ini}}) = \rho_{n,\text{ini}}(\boldsymbol{x}^{s}_{i}) \quad \text{for} \quad i = 1,2,\cdots,\tilde{N}^{s}, \tag{3.22}$$
$$T^{s}_{i}(t_{\text{ini}}) = T_{\text{ini}}(\boldsymbol{x}^{s}_{i}) \quad \text{for} \quad i = 1,2,\cdots,\tilde{N}^{s}, \tag{3.23}$$
$$\boldsymbol{v}^{\alpha}_{i}(t_{\text{ini}}) = \boldsymbol{v}_{\text{ini}}(\boldsymbol{x}^{\alpha}_{i}) \quad \text{for} \quad i = 1,2,\cdots,\tilde{N}^{\alpha}, \quad \alpha = 1,2. \tag{3.24}$$

The boundary conditions will be discussed in Section 4.

3.3 Numerical approximation of coupling conditions

In this section, the numerical approximation of the coupling conditions from Section 2.3 is described. For simplicity, we assume that $\tilde{\Omega}^{ff}$ is placed above Ω^{pm} and that the meshes covering the subdomains are defined in such a way that each s-node which lies on $\mathcal{I}$ corresponds to one of the nodes in $\mathcal{T}$ and vice versa (see Fig. 4, page 366).

3.3.1 Conditions (2.35), (2.40) and (2.42) for mass fraction X_n and temperature T

Due to the alignment of the spatial meshes, the use of conditions (2.35), (2.40) and (2.42) for the mass fraction of the NAPL vapor X_n in Eqs. (2.11) and (2.20) and for the temperature T in Eq. (2.22) is straightforward. At each interface node, we prescribe the function value at this node from the neighboring subdomain. Hence, in the example configuration depicted in Fig. 4 (page 366), we prescribe, e.g., $X_{n,3} := X^s_{n,2}$ (by (2.35)), $X^s_{n,2} := X_{n,3}$ (by (2.40)) and $T^s_2 := T_3$ (by (2.42)). The prescribed value is always from the latest time level which is available in the neighboring subdomain.

3.3.2 Condition (2.39) for shear stress

Employing coupling condition (2.39) for the shear stress in Eq. (2.21), all of the terms belonging to Ω^{pm} and Ω^{ff} are discretized in the same way as in Sections 3.1 and 3.2. The quantity on the discretized left-hand side is determined by the corresponding quantity on the right-hand side. Thus, at the node $\boldsymbol{x}^1_1$ in Fig. 4 (page 366), we have

$$2\sum_{l=1}^{2}\left[\boldsymbol{S}^1_{1,1}\right]_{k,l}\left[\boldsymbol{n}^1_{1,1}\right]_l\left[\boldsymbol{t}^1_{1,1}\right]_k := -\frac{\alpha_{\mathrm{BJ}}}{\sqrt{\left(\boldsymbol{t}^{\mathrm{T}}\boldsymbol{k}\boldsymbol{t}\right)_{1,2}}}\left(\left[\boldsymbol{v}^1_{1,1}-\boldsymbol{v}_{1,2}\right]_k\right)\left[\boldsymbol{t}^1_{1,1}\right]_k \tag{3.25}$$

for $k=1,2$. Again, the components of $\boldsymbol{v}_{1,2}$ are always from the latest time level which is available in Ω^{pm}.

3.3.3 Conditions (2.36) and (2.37) for mass flux of NAPL vapor and heat flux

Using coupling conditions (2.36) and (2.37) for the mass flux of the NAPL vapor in Eq. (2.11) and for the heat flux in Eq. (2.12), the approximations of the quantities on the right-hand sides are calculated (as in [1]) from the discretized versions of the corresponding conservation laws (i.e., from Eqs. (3.11) and (3.14)) which are considered at a time t and in which each of the time derivatives is approximated via the backward finite difference using the time step τ_{cou} (see Section 3.4). The resulting values are prescribed as $q^{b,n+1}_{X_n,\mathrm{Neu},i,j}$ and $q^{b,n+1}_{T,\mathrm{Neu},i,j}$, respectively, in (3.3) and (3.5) for all the time levels $t_{n+1}\in(t-\tau_{\mathrm{cou}},t]$ (see Section 3.4). Thus, according to Fig. 4 (page 366), the mass and heat fluxes going into

Ω^{pm} through the line segment connecting the nodes $\boldsymbol{x}_2^1$ and $\boldsymbol{x}_2^s$ (i.e., through $\Gamma_{3,2}^b$) are

$$\begin{aligned}
|\Gamma_{3,2}^b| q_{X_n,\mathrm{Neu},3,2}^{b,n+1} &:= -\frac{1}{2}|\Gamma_{2,1}^s| \underline{\rho_{n,2,1}^s}(t)\left(\boldsymbol{v}_{2,1}^s(t)+\boldsymbol{V}_{n,2,1}^s(t)\right)\cdot\boldsymbol{n}_{2,1}^s \\
&= \frac{|V_2^s|}{2}\frac{\rho_{n,2}^s(t)-\rho_{n,2}^s(t-\tau_{\mathrm{cou}})}{\tau_{\mathrm{cou}}} \\
&\quad +\frac{1}{2}\sum_{j\in\{0,2,3\}}|\Gamma_{2,j}^s|\underline{\rho_{n,2,j}^s(t)}\left(\boldsymbol{v}_{2,j}^s(t)+\boldsymbol{V}_{n,2,j}^s(t)\right)\cdot\boldsymbol{n}_{2,j}^s, \qquad (3.26)\\
|\Gamma_{3,2}^b| q_{T,\mathrm{Neu},3,2}^{b,n+1} &:= -\frac{1}{2}|\Gamma_{2,1}^s|\left[\boldsymbol{P}_{2,1}^s(t)\cdot\boldsymbol{v}_{2,1}^s(t)+\boldsymbol{Q}_{2,1}^s(t)+\underline{(\rho e)_{2,1}^s(t)}\,\boldsymbol{v}_{2,1}^s(t)\right]\cdot\boldsymbol{n}_{2,1}^s \\
&= \frac{|V_2^s|}{2}\frac{(\rho e)_2^s(t)-(\rho e)_2^s(t-\tau_{\mathrm{cou}})}{\tau_{\mathrm{cou}}}-\frac{|V_2^s|}{2}\boldsymbol{g}\cdot(\rho\boldsymbol{v})_2^s(t) \\
&\quad +\frac{1}{2}\sum_{j\in\{0,2,3\}}|\Gamma_{2,j}^s|\left[\boldsymbol{P}_{2,j}^s(t)\cdot\boldsymbol{v}_{2,j}^s(t)+\boldsymbol{Q}_{2,j}^s(t)+\underline{(\rho e)_{2,j}^s(t)}\,\boldsymbol{v}_{2,j}^s(t)\right]\cdot\boldsymbol{n}_{2,j}^s. \qquad (3.27)
\end{aligned}$$

Note that the factor $1/2$ in (3.26) and (3.27) follows from the fact that $2\cdot|\Gamma_{3,2}^b| = |\Gamma_{2,1}^s|$.

When applying the above procedure, the numerical fluxes through the parts of the boundary $\partial\tilde{\Omega}^{ff}$ not belonging to $\partial\Omega^{pm}$ (e.g., one half of the bottom side of V_1^s in Fig. 4, page 366) are considered to be zero.

3.3.4 Condition (2.34) for pressure p

Using coupling condition (2.34) for pressure p in Eq. (2.10), the quantity on the right-hand side at a given time t is approximated via the technique described in Section 3.3.3. However, this quantity consists of parts which are calculated from different equations ((3.12) and (3.13)) which correspond to different finite volumes (see Fig. 4, page 366). Therefore, these two parts are considered as values located at the midpoints of the bottom sides of the corresponding finite volumes V_i^1 and V_i^2, and the desired approximation is obtained by means of the linear interpolation from the nearest values. The resulting value is used as $p_{p,\mathrm{Dir},i}^{n+1}$ in (3.2) for all of the time levels $t_{n+1}\in(t-\tau_{\mathrm{cou}},t]$ (see Section 3.4). Note that due to the alignment of the spatial meshes, only the values calculated from (3.12) need to be interpolated because the node $\boldsymbol{x}_i\in\partial\Omega^{pm}$ is the midpoint of $\Gamma_{i,1}^2$, the bottom side of V_i^2. Thus, at the node $\boldsymbol{x}_2$ in Fig. 4 (page 366), we prescribe

$$p_{p,\mathrm{Dir},2}^{n+1} := \left(\left(\tilde{p}_{1,1}^1(t)+\tilde{p}_{2,1}^1(t)\right)/2\right)\left[\boldsymbol{n}_{1,1}^2\right]_1+\tilde{\tilde{p}}_{1,1}^2(t)\left[\boldsymbol{n}_{1,1}^2\right]_2, \qquad (3.28)$$

where the parts $\tilde{p}_{1,1}^1(t)$, $\tilde{p}_{2,1}^1(t)$ and $\tilde{\tilde{p}}_{1,1}^2(t)$ corresponding to the volumes V_1^1, V_2^1 and V_1^2, respectively, are given by

$$\begin{aligned}
\tilde{p}_{k,1}^1(t) &= \left[\boldsymbol{P}_{k,1}^1(t)\cdot\boldsymbol{n}_{k,1}^1\right]_1+\underline{(\rho v_1)_{k,1}^1(t)}\,\boldsymbol{v}_{k,1}^1(t)\cdot\boldsymbol{n}_{k,1}^1 \\
&= \frac{|V_k^1|}{|\Gamma_{k,1}^1|}\left(\rho_1^1(t)g_1-\frac{(\rho v_1)_k^1(t)-(\rho v_1)_k^1(t-\tau_{\mathrm{cou}})}{\tau_{\mathrm{cou}}}\right)
\end{aligned}$$

$$- \sum_{j\in\{0,2,3\}} \frac{|\Gamma^1_{k,j}|}{|\Gamma^1_{k,1}|}\left(\left[\boldsymbol{P}^1_{k,j}(t)\cdot\boldsymbol{n}^1_{k,j}\right]_1 + \underline{(\rho v_1)^1_{k,j}(t)}\,\boldsymbol{v}^1_{k,j}(t)\cdot\boldsymbol{n}^1_{k,j}\right) \quad \text{for} \quad k=1,2, \tag{3.29}$$

$$\begin{aligned}\tilde{\tilde{p}}^2_{1,1}(t) &= \left[\boldsymbol{P}^2_{1,1}(t)\cdot\boldsymbol{n}^2_{1,1}\right]_2 + \underline{(\rho v_2)^2_{1,1}(t)}\,\boldsymbol{v}^2_{1,1}(t)\cdot\boldsymbol{n}^2_{1,1}\\ &= \frac{|V^2_1|}{|\Gamma^2_{1,1}|}\left(\rho^2_1(t)g_2 - \frac{(\rho v_2)^2_1(t)-(\rho v_2)^2_1(t-\tau_{\text{cou}})}{\tau_{\text{cou}}}\right)\\ &\quad - \sum_{j\in\{0,2,3\}} \frac{|\Gamma^2_{1,j}|}{|\Gamma^2_{1,1}|}\left(\left[\boldsymbol{P}^2_{1,j}(t)\cdot\boldsymbol{n}^2_{1,j}\right]_2 + \underline{(\rho v_2)^2_{1,j}(t)}\,\boldsymbol{v}^2_{1,j}(t)\cdot\boldsymbol{n}^2_{1,j}\right).\end{aligned} \tag{3.30}$$

3.3.5 Conditions (2.38) and (2.41) for mass fluxes

Coupling conditions (2.38) and (2.41) for the mass fluxes in Eqs. (2.19) and (2.20) are utilized in the same way as conditions (2.36) and (2.37) (see Section 3.3.3). The approximations of the quantities on the right-hand sides are calculated from the equations which are obtained by discretizing Eqs. (2.1) and (2.2) considered at a time t by means of the same discretization techniques as in Section 3.1, i.e., from equations

$$\begin{aligned}&\sum_{e\in\Lambda^n_i} |V^e_i|\phi_e \frac{\rho_i(t)-\rho_i(t-\tau_{\text{cou}})}{\tau_{\text{cou}}} + \sum_{j\in\Lambda_i}\sum_{e\in\Lambda_{i,j}} \left|\Gamma^e_{i,j}\right| \rho^e_{i,j}(t)\boldsymbol{v}^e_{i,j}(t)\cdot\boldsymbol{n}^e_{i,j}\\ &\quad + \sum_{j\in\Lambda^b_i} \left|\Gamma^b_{i,j}\right| \rho^b_{i,j}(t)\boldsymbol{v}^b_{i,j}(t)\cdot\boldsymbol{n}^b_{i,j} = \sum_{e\in\Lambda^n_i} |V^e_i| F_i(t),\end{aligned} \tag{3.31}$$

$$\begin{aligned}&\sum_{e\in\Lambda^n_i} |V^e_i|\phi_e \frac{\rho_{n,i}(t)-\rho_{n,i}(t-\tau_{\text{cou}})}{\tau_{\text{cou}}}\\ &\quad + \sum_{j\in\Lambda_i}\sum_{e\in\Lambda_{i,j}} \left|\Gamma^e_{i,j}\right| \rho^e_{i,j}(t)\boldsymbol{n}^e_{i,j}\cdot\left(\underline{X^e_{n,i,j}(t)}\boldsymbol{v}^e_{i,j}(t) - D^e_{i,j}(t)\nabla X^e_{n,i,j}(t)\right)\\ &\quad + \sum_{j\in\Lambda^b_i} \left|\Gamma^b_{i,j}\right| \rho^b_{i,j}(t)\boldsymbol{n}^b_{i,j}\cdot\left(X^b_{n,i,j}(t)\boldsymbol{v}^b_{i,j}(t) - D^b_{i,j}(t)\nabla X^b_{n,i,j}(t)\right) = \sum_{e\in\Lambda^n_i} |V^e_i| F_{n,i}(t).\end{aligned} \tag{3.32}$$

The resulting values are prescribed in Eqs. (3.10) and (3.11) instead of the terms representing the numerical fluxes through the bottom side of the corresponding boundary finite volume V^s_i for all times $\tilde{t}\in[t,t+\tau_{\text{cou}})$ (see Section 3.4). Consequently, in the case of the mass flux of the mixture and the mass flux of the NAPL vapor through $\partial V^s_2\cap\partial V_3$ in Fig. 4 (page 366), we have

$$\begin{aligned}|\Gamma^s_{2,1}|\underline{\rho^s_{2,1}}(\tilde{t})\boldsymbol{v}^s_{2,1}(\tilde{t})\cdot\boldsymbol{n}^s_{2,1} &:= -\sum_{j\in\Lambda^b_3} \left|\Gamma^b_{3,j}\right| \rho^b_{3,j}(t)\boldsymbol{v}^b_{3,j}(t)\cdot\boldsymbol{n}^b_{3,j} = \sum_{e\in\Lambda^n_3} |V^e_3|\phi_e \frac{\rho_3(t)-\rho_3(t-\tau_{\text{cou}})}{\tau_{\text{cou}}}\\ &\quad + \sum_{j\in\Lambda_3}\sum_{e\in\Lambda_{3,j}} \left|\Gamma^e_{3,j}\right| \rho^e_{3,j}(t)\boldsymbol{v}^e_{3,j}(t)\cdot\boldsymbol{n}^e_{3,j} - \sum_{e\in\Lambda^n_3} |V^e_3| F_3(t),\end{aligned} \tag{3.33}$$

$$
\begin{aligned}
&|\Gamma^s_{2,1}|\underline{\rho^s_{n,2,1}(\tilde{t})}\left(\boldsymbol{v}^s_{2,1}(\tilde{t})+\boldsymbol{V}^s_{n,2,1}(\tilde{t})\right)\cdot\boldsymbol{n}^s_{2,1}\\
&:=-\sum_{j\in\Lambda^b_3}\left|\Gamma^b_{3,j}\right|\rho^b_{3,j}(t)\boldsymbol{n}^b_{3,j}\cdot\left(X^b_{n,3,j}(t)\boldsymbol{v}^b_{3,j}(t)-D^b_{3,j}(t)\nabla X^b_{n,3,j}(t)\right)\\
&=\sum_{e\in\Lambda^n_3}|V^e_3|\phi_e\frac{\rho_{n,3}(t)-\rho_{n,3}(t-\tau_{\text{cou}})}{\tau_{\text{cou}}}\\
&\quad+\sum_{j\in\Lambda_3}\sum_{e\in\Lambda_{3,j}}\left|\Gamma^e_{3,j}\right|\rho^e_{3,j}(t)\boldsymbol{n}^e_{3,j}\cdot\left(\underline{X^e_{n,3,j}(t)}\boldsymbol{v}^e_{3,j}(t)-D^e_{3,j}(t)\nabla X^e_{n,3,j}(t)\right)\\
&\quad-\sum_{e\in\Lambda^n_3}|V^e_3|F_{n,3}(t).
\end{aligned}
\tag{3.34}
$$

3.3.6 Condition (2.38) for momentum ρv in Eq. (3.13)

Finally, when using coupling condition (2.38) for Eq. (3.13), we calculate the term

$$
\sum_{j\in\Lambda^b_i}\left|\Gamma^b_{i,j}\right|\rho^b_{i,j}(t)\boldsymbol{v}^b_{i,j}(t)\cdot\boldsymbol{n}^b_{i,j}
\tag{3.35}
$$

from Eq. (3.31) and assume that

$$
|\Gamma^2_{k,1}|\left(|\left[\rho^2_{k,1}(\tilde{t})\boldsymbol{v}^2_{k,1}(\tilde{t})\right]_1\left[\boldsymbol{n}^2_{k,1}\right]_1+\left[\rho^2_{k,1}\boldsymbol{v}^2_{k,1}(\tilde{t})\right]_2\left[\boldsymbol{n}^2_{k,1}\right]_2\right)=-\sum_{j\in\Lambda^b_i}\left|\Gamma^b_{i,j}\right|\rho^b_{i,j}(t)\boldsymbol{v}^b_{i,j}(t)\cdot\boldsymbol{n}^b_{i,j}
\tag{3.36}
$$

for boundary finite volumes V^2_k and V_i such that $\Gamma^2_{k,1}=\Gamma^b_i$ (e.g., the volumes V^2_1 and V_2 in Fig. 4) and for all times $\tilde{t}\in[t,t+\tau_{\text{cou}})$ (see Section 3.4). Considering the fact that the first term in (3.36) can be obtained independently of the second one by solving (3.12), we can prescribe

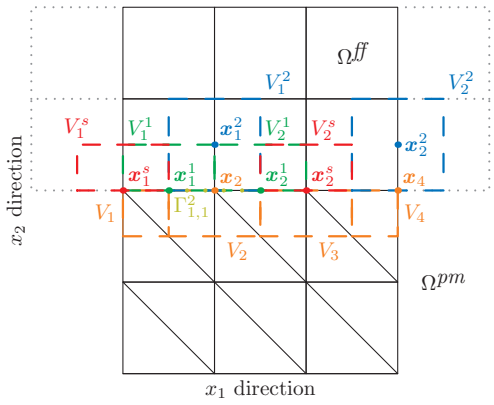

Figure 4: Structure of spatial meshes covering $\overline{\Omega}^{pm}\cup\overline{\tilde{\Omega}}^{ff}$ in the simulations. The dotted lines denote the auxiliary parts of the meshes and $\Gamma^2_{1,1}$, the bottom side of the volume V^2_1. Note that $\boldsymbol{x}_1=\boldsymbol{x}^s_1$, $\boldsymbol{x}_3=\boldsymbol{x}^s_2$ and $\Gamma^b_2=\Gamma^2_{1,1}$.

$$\left[\rho^2_{k,1}(\tilde{t})v^2_{k,1}(\tilde{t})\right]_2 := \frac{-1}{|\Gamma^2_{k,1}|\left[\boldsymbol{n}^2_{k,1}\right]_2}\left(\sum_{j\in\Lambda^b_i}\left|\Gamma^b_{i,j}\right|\rho^b_{i,j}(t)\boldsymbol{v}^b_{i,j}(t)\cdot\boldsymbol{n}^b_{i,j}+|\Gamma^2_{k,1}|\left[\rho^2_{k,1}(\tilde{t})\boldsymbol{v}^2_{k,1}(\tilde{t})\right]_1\left[\boldsymbol{n}^2_{k,1}\right]_1\right). \tag{3.37}$$

But since there are not any 2-nodes on $\Gamma^2_{k,1}$ (see the edge $\Gamma^2_{1,1}$ in Fig. 4), the value of the right-hand side of (3.37) is prescribed as $(\rho v_2)^2_k(\tilde{t})$. Hence, at the node x^2_1 in Fig. 4, we have

$$(\rho v_2)^2_1(\tilde{t}) := \frac{-1}{|\Gamma^2_{1,1}|\left[\boldsymbol{n}^2_{1,1}\right]_2}\left(\sum_{j\in\Lambda^b_2}\left|\Gamma^b_{2,j}\right|\rho^b_{2,j}(t)\boldsymbol{v}^b_{2,j}(t)\cdot\boldsymbol{n}^b_{2,j}+|\Gamma^2_{1,1}|\left[\rho^2_{1,1}(\tilde{t})\boldsymbol{v}^2_{1,1}(\tilde{t})\right]_1\left[\boldsymbol{n}^2_{1,1}\right]_1\right). \tag{3.38}$$

3.4 Coupling of numerical schemes

In this section, we summarize how the numerical schemes from Sections 3.1 and 3.2 are coupled via the conditions from Section 3.3. Assume that $[t_{\rm ini},t_{\rm fin}]$ is discretized by means of a sequence $(t_n)_{n=0}^{N_t}$, where $t_{n+1}-t_n=\tau_{\rm cou}$. The realization of the coupling can be described by the following algorithm:

1. Calculate the initial conditions for the model of coupled flows by finding the numerical solutions of the submodels from Sections 3.1 and 3.2 on a time interval $[t_{\rm ini},t_{\rm fin}]$, where the submodels are solved uncoupled under stationary conditions. Here the values $t_{\rm ini}$ and $t_{\rm fin}$ are temporary values which are not related to the actual initial and final time introduced on page 352 and which are used only in this step. This preparation is necessary because the initial conditions for Ω^{ff} need to be close to steady state. Since the submodels are uncoupled, we use the following boundary conditions on the interface $\mathcal{I}$ (cf. Section 2.3) for all $t\in[t_{\rm ini},t_{\rm fin}]$ and $\boldsymbol{x}\in\mathcal{I}$:

$$p^{pm}(t,\boldsymbol{x}) := p^{pm}_{\rm ini}(\boldsymbol{x}), \quad \left[\left(\rho c_p T\boldsymbol{v}-\lambda_m\nabla T\right)\cdot\boldsymbol{n}\right]^{pm}(t,\boldsymbol{x}) := 0, \tag{3.39}$$

$$X^{pm}_n(t,\boldsymbol{x}) := X^{pm}_{n,\rm ini}(\boldsymbol{x}) \quad \text{or} \quad \left[(X_n\rho\boldsymbol{v}-D\rho\nabla X_n)\cdot\boldsymbol{n}\right]^{pm}(t,\boldsymbol{x}) := 0, \tag{3.40}$$

$$\left(2[\boldsymbol{Sn}]^{ff}(t,\boldsymbol{x})\right)\cdot\boldsymbol{t} := \left(-\frac{\alpha_{\rm BJ}}{\sqrt{\boldsymbol{t}^{\rm T}\boldsymbol{k}\boldsymbol{t}}}\boldsymbol{v}^{ff}(t,\boldsymbol{x})\right)\cdot\boldsymbol{t}, \tag{3.41}$$

$$[\rho\boldsymbol{v}\cdot\boldsymbol{n}]^{ff}(t,\boldsymbol{x}) := 0, \quad T^{ff}(t,\boldsymbol{x}) := T^{ff}_{\rm ini}(\boldsymbol{x}), \tag{3.42}$$

$$X^{ff}_n(t,\boldsymbol{x}) := \rho^{ff}_{n,\rm ini}(\boldsymbol{x})/\rho^{ff}_{\rm ini}(\boldsymbol{x}) \quad \text{or} \quad \left[(\rho_n(\boldsymbol{v}+\boldsymbol{V}_n))\cdot\boldsymbol{n}\right]^{ff}(t,\boldsymbol{x}) := 0, \tag{3.43}$$

   where we use the combination of the conditions in Eqs. (3.40) and (3.43) which corresponds to our choice of the conditions from Eqs. (2.35), (2.36), (2.40) and (2.41).

2. Set the index of the time level $n := 0$ and use the values of the state variables from the final time of the simulation in step 1 as the initial conditions for the solution of the numerical submodels from Sections 3.1 and 3.2 on the time interval $[t_{\rm ini},t_{\rm fin}]$ (i.e., as the solution at time $t=t_{\rm ini}$).

3. Using the discretized versions of coupling conditions from Section 3.3, calculate the values which are to be prescribed at $\mathcal{I}$ for Ω^{ff} for times $t \in [t_n, t_{n+1})$. If $t_n = t_{\text{ini}}$, use the conditions from Section 3.3 modified in the same way as in step 1.

4. Solve the numerical submodel from Section 3.2 on the time interval $[t_n, t_{n+1}]$ using the boundary conditions at $\mathcal{I}$ from step 3.

5. Using the discretized versions of coupling conditions from Section 3.3, calculate the values which are to be prescribed at $\mathcal{I}$ for Ω^{pm} for times $t \in [t_n, t_{n+1})$.

6. Solve the numerical submodel from Section 3.1 on the time interval $[t_n, t_{n+1}]$ using the boundary conditions at $\mathcal{I}$ from step 5.

7. If $t_{n+1} \neq t_{\text{fin}}$, increase n by one and go to step 3. If $t_{n+1} = t_{\text{fin}}$, then at interface nodes, prescribe the latest solution values. (This is done because each of the submodels has its own interface values.) Then stop.

Note that although the algorithm from Section 3.2 is used prior to the one from Section 3.1 on each time interval $[t_n, t_{n+1}]$, these algorithms can be used in the reverse order too (as in Test 2 in Section 4.1).

4 Computational studies

In this section, we present the results of several numerical tests which model flow in a tank filled with sand and in the free space of atmospheric flow above its surface. This setup corresponds to the laboratory experiments reported in [8] and [13].

In these tests, we used the following setup: The subdomains are defined as $\Omega^{pm} = (0,3) \times (-1,0)$ and $\Omega^{ff} = (0,3) \times (0,1)$ (see Fig. 5, page 370). Many physical parameters in the numerical model have the same constant values in all the tests. These values as well as the rest of the parameter values mentioned in this paragraph are listed (together with their units) in Table 1. The permeability tensor $\boldsymbol{k}$ is a scalar multiple of the identity tensor, i.e., $\boldsymbol{k} = \tilde{k}\boldsymbol{I}$, where $\tilde{k}$ varies between $\tilde{k}_1$ and $\tilde{k}_2$ (see Fig. 7, page 380). The porosity ϕ and density ρ_s vary linearly with $\tilde{k}$ between ϕ_1 and ϕ_2 and between $\rho_{s,1}$ and $\rho_{s,2}$, respectively. Finally, based on information in [6], the coefficient k_{Tn} is defined as

$$k_{Tn} = 0.077 X_n X_g. \tag{4.1}$$

In step 1 of the algorithm in Section 3.4, we always considered $t_{\text{ini}} = 0$ and $t_{\text{fin}} = 1$, where the values are in seconds. The initial conditions for time t_{ini} in step 1 were always

Table 1: Values of constant physical parameters. The values for the gas and NAPL vapor correspond to the values for the air and trichloroethylene [22], respectively. The values for the porous medium are selected based on the values listed in [3] and [27]. The values of $D_{g,n}$, $D_{g,g}$, $D_{n,n}$, k_{Tg} and k_{Tn} are calculated via Eq. (2.28) and the formula $k_{Tn}=-k_{Tg}$, where k_{Tn} is given by Eq. (4.1).

parameter	value	units	parameter	value	units
μ	$1.81\cdot10^{-5}$	$\mathrm{kg\cdot m^{-1}\cdot s^{-1}}$	a	0.01	m
M_g	0.02896	$\mathrm{kg\cdot mol^{-1}}$	$\rho_{s,1}$	1500.0	$\mathrm{kg\cdot m^{-3}}$
M_n	0.13139	$\mathrm{kg\cdot mol^{-1}}$	$\rho_{s,2}$	1590.0	$\mathrm{kg\cdot m^{-3}}$
R	8.3144621	$\mathrm{J\cdot K^{-1}\cdot mol^{-1}}$	c_s	830.0	$\mathrm{m^2\cdot s^{-2}\cdot K^{-1}}$
g_1	0	$\mathrm{m\cdot s^{-2}}$	$c_{p,g}$	1005.0	$\mathrm{m^2\cdot s^{-2}\cdot K^{-1}}$
g_2	-9.81	$\mathrm{m\cdot s^{-2}}$	$c_{p,n}$	1300.0	$\mathrm{m^2\cdot s^{-2}\cdot K^{-1}}$
F	0	$\mathrm{kg\cdot m^{-3}\cdot s^{-1}}$	$c_{V,g}$	718.0	$\mathrm{m^2\cdot s^{-2}\cdot K^{-1}}$
F_n	0	$\mathrm{kg\cdot m^{-3}\cdot s^{-1}}$	$c_{V,n}$	975.0	$\mathrm{m^2\cdot s^{-2}\cdot K^{-1}}$
ϕ_1	0.399	–	λ_s	0.2	$\mathrm{kg\cdot m\cdot s^{-3}\cdot K^{-1}}$
ϕ_2	0.433	–	λ	0.024	$\mathrm{kg\cdot m\cdot s^{-3}\cdot K^{-1}}$
$\tilde{k}_1$	$2.0\cdot10^{-9}$	$\mathrm{m^2}$	q_s	0	$\mathrm{kg\cdot m^{-1}\cdot s^{-3}}$
$\tilde{k}_2$	$2.0\cdot10^{-11}$	$\mathrm{m^2}$	q	0	$\mathrm{kg\cdot m^{-1}\cdot s^{-3}}$
D_n	$8.35\cdot10^{-6}$	$\mathrm{m^2\cdot s^{-1}}$	α_{BJ}	1.0	–
$D_{n,g}$	$8.35\cdot10^{-6}$	$\mathrm{m^2\cdot s^{-1}}$	p_0	101325.0	Pa

the following:

$$T_{\mathrm{ini}}(\boldsymbol{x})=T_0^{pm},\quad X_{n,\mathrm{ini}}(\boldsymbol{x})=X_{n,0}^{pm},\quad p_{\mathrm{ini}}(\boldsymbol{x})=p_0\exp\left(\frac{M_0^{pm}g_2(x_2-0.5)}{RT_0^{pm}}\right)\quad\forall\boldsymbol{x}\in\overline{\Omega}^{pm},$$

$$\text{where}\quad M_0^{pm}=\left(X_{n,0}^{pm}/M_n+(1-X_{n,0}^{pm})/M_g\right)^{-1};$$

$$T_{\mathrm{ini}}(\boldsymbol{x})=T_0^{ff},\quad \rho_{\mathrm{ini}}(\boldsymbol{x})=\frac{p_0M_0^{ff}}{RT_0^{ff}}\exp\left(\frac{M_0^{ff}g_2(x_2-0.5)}{RT_0^{ff}}\right),\quad \rho_{n,\mathrm{ini}}(\boldsymbol{x})=X_{n,0}^{ff}\rho_{\mathrm{ini}}(\boldsymbol{x}),$$

$$v_{1,\mathrm{ini}}(\boldsymbol{x})=v_{1,0}x_2x_2,\quad v_{2,\mathrm{ini}}(\boldsymbol{x})=0\quad\forall\boldsymbol{x}\in\overline{\tilde{\Omega}}^{ff},$$

$$\text{where}\quad M_0^{ff}=\left(X_{n,0}^{ff}/M_n+(1-X_{n,0}^{ff})/M_g\right)^{-1}.$$

The constants T_0^{pm}, $X_{n,0}^{pm}$, T_0^{ff}, $X_{n,0}^{ff}$ and $v_{1,0}$ in the above formulas will be specified in the description of each test. The value of p_0 is the same in all tests. It is listed in Table 1. Remark that the initial conditions for $\overline{\Omega}^{pm}$ represent hydrostatic conditions at constant temperature T_0^{pm} and mass fraction $X_{n,0}^{pm}$.

In all the tests, $\partial\Omega$ was divided into several parts on which different boundary conditions were prescribed (see Figs. 5 and 6, pages 370 and 371). In the following list, the

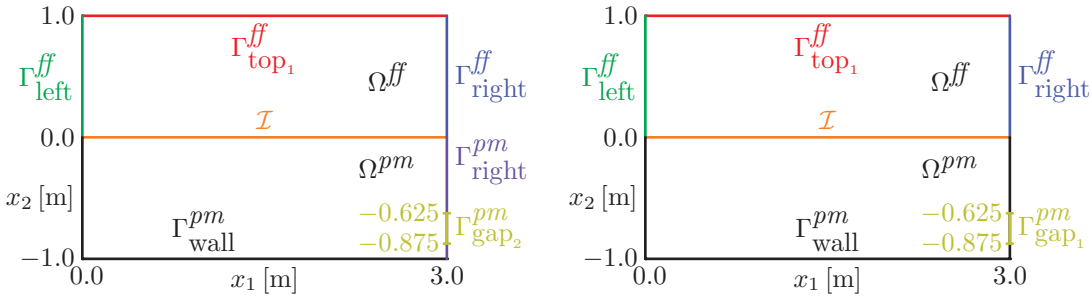

(a) Division of $\partial\Omega$ in Tests 1–4.

(b) Division of $\partial\Omega$ in Tests 5 and 6.

Figure 5: Division of $\partial\Omega$ in Tests 1–6. The vertical coordinates of the endpoints of $\Gamma^{pm}_{\text{gap}_1}$, $\Gamma^{pm}_{\text{gap}_2}$ are $x_2=-0.625$ and $x_2=-0.875$. In Test 6, $\Gamma^{pm}_{\text{gap}_1}$ was replaced by $\Gamma^{pm}_{\text{wall}}$.

'extrapolation' means that on $\partial\Omega^{ff}$, the new values of the numerical solution are calculated via extrapolation from the new values of the numerical solution which we already have in the interior of Ω^{ff}. For $\partial\Omega^{ff}$, we considered these parts:

- $\Gamma^{ff}_{\text{left}}$: For all $t\in[t_{\text{ini}},t_{\text{fin}}]$, we prescribe

$$\rho(t,\boldsymbol{x})=\rho_{\text{ini}}(\boldsymbol{x}),\quad \rho_n(t,\boldsymbol{x})=X^{ff}_{n,0}\rho(t,\boldsymbol{x}),\quad \boldsymbol{v}(t,\boldsymbol{x})=\boldsymbol{v}_{\text{ini}}(\boldsymbol{x})\quad \forall\boldsymbol{x}\in\Gamma^{ff}_{\text{left}}$$

  for step 1 of the algorithm in Section 3.4,

$$\rho(t,\boldsymbol{x})=p_1\frac{\rho_{\text{ini}}(\boldsymbol{x})}{p_0},\quad \rho_n(t,\boldsymbol{x})=X_{n,1}\rho(t,\boldsymbol{x}),\quad \boldsymbol{v}(t,\boldsymbol{x})=\boldsymbol{v}_{\text{ini}}(\boldsymbol{x})\quad \forall\boldsymbol{x}\in\Gamma^{ff}_{\text{left}}\quad \text{otherwise,}$$

  and using the constant extrapolation, we extrapolate p from the interior of Ω^{ff}.

- $\Gamma^{ff}_{\text{top}_1}$: We prescribe $\boldsymbol{v}(t,\boldsymbol{x})=\boldsymbol{v}_{\text{ini}}(\boldsymbol{x})\ \forall\boldsymbol{x}\in\Gamma^{ff}_{\text{top}_1}$, $t\in[t_{\text{ini}},t_{\text{fin}}]$ and we extrapolate ρ and p using the linear extrapolation and X_n using the constant extrapolation from the interior of Ω^{ff}.

- $\Gamma^{ff}_{\text{top}_2}$: We prescribe $\boldsymbol{v}(t,\boldsymbol{x})=\boldsymbol{v}_{\text{ini}}(\boldsymbol{x})\ \forall\boldsymbol{x}\in\Gamma^{ff}_{\text{top}_2}$, $t\in[t_{\text{ini}},t_{\text{fin}}]$ and we extrapolate ρ using the linear extrapolation and ρ_n and T using the constant extrapolation from the interior of Ω^{ff}.

- $\Gamma^{ff}_{\text{right}}$: We prescribe $p(t,\boldsymbol{x})=p_0\exp\left(M^{ff}_0 g_2(x_2-0.5)/(RT^{ff}_0)\right)\ \forall\boldsymbol{x}\in\Gamma^{ff}_{\text{right}}$, $t\in[t_{\text{ini}},t_{\text{fin}}]$ and we extrapolate ρ, ρ_n and v_2 using the constant extrapolation and we solve (3.12).

- $\Gamma^{ff}_{\text{side}}$: We prescribe $\boldsymbol{v}(t,\boldsymbol{x})=\boldsymbol{v}_{\text{ini}}(\boldsymbol{x})\ \forall\boldsymbol{x}\in\Gamma^{ff}_{\text{side}}$, $t\in[t_{\text{ini}},t_{\text{fin}}]$ and we extrapolate ρ, ρ_n and T using the constant extrapolation from the interior of Ω^{ff}.

- $\mathcal{I}$: This part is described in Sections 3.3 and 3.4.

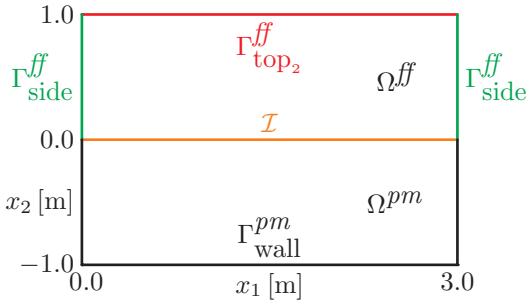

Figure 6: Division of $\partial\Omega$ in Test 7.

The constants p_1 and $X_{n,1}$ in the above list will be specified later on. We note that in the numerical tests presented in this text, the original domain Ω^{ff} was extended by one layer of auxiliary rectangles on the left- and right-hand side (see Fig. 4, page 366). Therefore, the boundary conditions for $\Gamma^{ff}_{\text{left}}$, $\Gamma^{ff}_{\text{right}}$ and $\Gamma^{ff}_{\text{side}}$ were prescribed at the dummy nodes, and the boundaries $\Gamma^{ff}_{\text{top}_1}$ and $\Gamma^{ff}_{\text{top}_2}$ were extended. The corner nodes were considered to be parts of $\Gamma^{ff}_{\text{left}}$, $\Gamma^{ff}_{\text{right}}$ and $\Gamma^{ff}_{\text{side}}$.

For $\partial\Omega^{pm}$, the following parts were considered (see Figs. 5 and 6, pages 370 and 371):

- $\Gamma^{pm}_{\text{wall}}$: We assume that $\Gamma^{pm}_{\text{wall}}$ is a subset of $\Gamma_{p,\text{Neu}}$, $\Gamma_{X_n,\text{Neu}}$ and $\Gamma_{T,\text{Neu}}$ and we set

$$q_{p,\text{Neu}}(t,\boldsymbol{x})=0,\quad q_{X_n,\text{Neu}}(t,\boldsymbol{x})=0,\quad q_{T,\text{Neu}}(t,\boldsymbol{x})=0\quad \forall \boldsymbol{x}\in\Gamma^{pm}_{\text{wall}},\quad t\in[t_{\text{ini}},t_{\text{fin}}].$$

- $\Gamma^{pm}_{\text{gap}_1}$: We assume that $\Gamma^{pm}_{\text{gap}_1}$ is a subset of $\Gamma_{p,\text{Neu}}$, $\Gamma_{X_n,\text{out}}$ and $\Gamma_{T,\text{out}}$. For all $t\in[t_{\text{ini}},t_{\text{fin}}]$, we set

$$\begin{aligned} &q_{p,\text{Neu}}(t,\boldsymbol{x})=0 && \forall \boldsymbol{x}\in\Gamma^{pm}_{\text{gap}_1} && \text{for step 1 of the algorithm in Section 3.4,}\\ &q_{p,\text{Neu}}(t,\boldsymbol{x})=10^{-3} && \forall \boldsymbol{x}\in\Gamma^{pm}_{\text{gap}_1} && \text{otherwise.}\end{aligned}$$

- $\Gamma^{pm}_{\text{gap}_2}$: We assume that $\Gamma^{pm}_{\text{gap}_2}$ is a subset of $\Gamma_{p,\text{Dir}}$, $\Gamma_{X_n,\text{Dir}}$ and $\Gamma_{T,\text{Dir}}$. For all $t\in[t_{\text{ini}},t_{\text{fin}}]$, we set

$$\begin{aligned} &p_{p,\text{Dir}}(t,\boldsymbol{x})=p_{\text{ini}}(\boldsymbol{x}) && \forall \boldsymbol{x}\in\Gamma^{pm}_{\text{gap}_2} && \text{for step 1 of the algorithm in Section 3.4,}\\ &p_{p,\text{Dir}}(t,\boldsymbol{x})=\frac{p_2}{p_0}p_{\text{ini}}(\boldsymbol{x}) && \forall \boldsymbol{x}\in\Gamma^{pm}_{\text{gap}_2} && \text{otherwise,}\\ &X_{nX_n,\text{Dir}}(t,\boldsymbol{x})=X_{n,\text{ini}}(\boldsymbol{x}),\quad T_{T,\text{Dir}}(t,\boldsymbol{x})=T_{\text{ini}}(\boldsymbol{x}) && \forall \boldsymbol{x}\in\Gamma^{pm}_{\text{gap}_2}, && \end{aligned}$$

  where the constant p_2 will be specified later on.

- $\Gamma^{pm}_{\text{right}}$: We assume that $\Gamma^{pm}_{\text{right}}$ is a subset of $\Gamma_{p,\text{Dir}}$, $\Gamma_{X_n,\text{Dir}}$ and $\Gamma_{T,\text{Dir}}$ and we set

$$p_{p,\text{Dir}}=p_{\text{ini}}(\boldsymbol{x}),\quad X_{nX_n,\text{Dir}}(t,\boldsymbol{x})=X_{n,\text{ini}}(\boldsymbol{x}),\quad T_{T,\text{Dir}}(t,\boldsymbol{x})=T_{\text{ini}}(\boldsymbol{x}), \tag{4.2}$$

$$\forall \boldsymbol{x}\in\Gamma^{pm}_{\text{right}},\quad t\in[t_{\text{ini}},t_{\text{fin}}]. \tag{4.3}$$

- $\mathcal{I}$: This part is described in Sections 3.3 and 3.4.

All the results presented here were obtained using the numerical algorithm described in this paper. This algorithm was implemented in the C++ programming language and parallelized via OpenMP. The computations were performed on a computer with 4 core Intel Core i5-2500 CPU 3.30 GHz, 7.8 GB RAM.

The remaining details of the computational tests are presented in the following sections.

4.1 Quantitative computational studies

In order to assess the reliability of our numerical model, we chose several reference experimental setups and for each setup, we carried out simulations with differently fine spatial meshes. Then, we measured the difference between the respective numerical solutions and a numerical solution on a very fine mesh ('fine solution').

The fineness of the spatial meshes was characterized by the parameter h denoting the largest circumdiameter of all the mesh cells. Given a corresponding solution z_h and a fine solution z_{fine}, the difference $\|z_h - z_{\text{fine}}\|_t$ between these solutions ('error') was measured as

$$\|z_h - z_{\text{fine}}\|_t = \max_{j=0,\cdots,N} \left\{ \|z_h(t_{\text{ini}} + j\nu) - z_{\text{fine}}(t_{\text{ini}} + j\nu)\|_\xi \right\}, \tag{4.4}$$

where ν denotes the output time step, N stands for the number of the output time steps ($t_{\text{ini}} + N\nu = t_{\text{fin}}$), and $\|z_h(t) - z_{\text{fine}}(t)\|_\xi$ is one of the norms

$$\|z_h(t) - z_{\text{fine}}(t)\|_{l_1} = \sum_{k=1,\cdots,N_{\text{ref}}} |V_k| \cdot \left| z_h^k(t) - z_{\text{fine}}^k(t) \right|, \tag{4.5}$$

$$\|z_h(t) - z_{\text{fine}}(t)\|_{l_2} = \sqrt{\sum_{k=1,\cdots,N_{\text{ref}}} |V_k| \cdot \left| z_h^k(t) - z_{\text{fine}}^k(t) \right|^2}, \tag{4.6}$$

where $z_h^k(t)$ and $z_{\text{fine}}^k(t)$ denote the k-th nodal values of the projections of $z_h(t)$ and $z_{\text{fine}}(t)$ onto a regular orthogonal mesh ('reference mesh') with N_{ref} nodes, and $|V_k|$ is the area of the finite volume associated with the k-th node of the reference mesh. The mesh for the measurement of the error in $\overline{\Omega}^{pm}$ had the same structure as the mesh depicted in Fig. 2 (page 356). In the case of $\overline{\Omega}^{ff}$, the mesh with the structure of the mesh of rectangles in Fig. 3 (page 360) was considered for all variables. Both meshes were uniform.

The resulting errors were compared by calculating the experimental order of convergence (EOC) [10], i.e., the coefficient α_{EOC} from the formula

$$\frac{\|z_{h_1} - z_{\text{fine}}\|_t}{\|z_{h_2} - z_{\text{fine}}\|_t} = \left(\frac{h_1}{h_2} \right)^{\alpha_{\text{EOC}}}, \tag{4.7}$$

where h_1 and h_2 are two different values of h.

Table 2: Mesh parameters in Tests 1–7. According to the definition of h, we have $h=\sqrt{h_{x_1}^2+h_{x_2}^2}$.

mesh number	h_{x_1}	h_{x_2}	τ	τ_{cou}
1	3/24	1/16	1/16	1/8
2	3/49	1/33	1/64	1/16
3	3/99	1/67	1/256	1/32
4	3/192	1/128	1/1024	1/64

In all of the computations, we chose $t_{\text{ini}}=0$ and $t_{\text{fin}}=120$ (where the values are in seconds), and the errors were measured with $\nu=1$ separately for $\overline{\Omega}^{pm}$ and $\overline{\Omega}^{ff}$. The triangulation of $\overline{\Omega}^{pm}$ had the same structure as the triangulation depicted in Fig. 2 (page 356). In the case of $\overline{\Omega}^{ff}$, the mesh with the same structure as the mesh of rectangles in Fig. 3 (page 360) was employed. Both meshes were uniform. The spatial steps in x_1- and x_2-direction, h_{x_1} and h_{x_2} (they were the same in both subdomains) together with the time step for coupling, τ_{cou}, and the time step for Ω^{pm}, τ, are listed in Table 2. Note that for our choice of spatial meshes, we have $h=\sqrt{h_{x_1}^2+h_{x_2}^2}$. Also note that the values of the steps h_{x_1} and h_{x_2} are chosen in such a way that on each mesh, the numerical approximations of the line segment $\Gamma_{\text{gap}_2}^{pm}$ and the regions of low permeability (in Test 4) slightly differ. The reason for this choice was that we wanted to avoid superconvergence.

The numerical solution corresponding to mesh 4 was considered as the fine solution. The spatial steps of the reference mesh were $h_{x_1}=1/384$ and $h_{x_2}=1/256$. The boundary $\partial\Omega$ was always divided as in Fig. 5a. The runtimes for the meshes 1, 2, 3 and 4 were approximately 15 min, 2 h, 17 h and 7 days, respectively.

The EOC measurements were carried out in four tests which are described in Sections 4.1.1–4.1.4. Their results are discussed in Section 4.1.5.

4.1.1 Test 1

This test models the escape of NAPL vapor from soil through its surface under the heating of this soil in the case where there is flow inside the soil which is not induced by the atmospheric flow above the soil surface and which affects this atmospheric flow.

- Particular test setting: $T_0^{pm}=290.15$, $X_{n,0}^{pm}=10^{-3}$, $T_0^{ff}=295.15$, $v_{1,0}=20.0$, $p_1=p_0$, $p_2=101315.0$, $X_{n,0}^{ff}=0$ and $X_{n,1}=X_{n,0}^{ff}$. The soil is homogeneous. Its properties correspond to the parameter values with the subscript 1 in Table 1, page 369.
- Particular coupling conditions: Condition (2.36) is used for the mass flux of the NAPL vapor in (2.11). Condition (2.40) is used for the mass fraction of the NAPL vapor X_n in (2.20).

The resulting errors and corresponding EOC coefficients are listed in Tables 3 and 4, pages 374 and 375.

Table 3: Errors and experimental orders of convergence (EOCs) for $\overline{\Omega}^{pm}$ for Test 1.

p in $\overline{\Omega}^{pm}$				
mesh number	error l_2	EOC l_2	error l_1	EOC l_1
1	$5.097927 \cdot 10^{-1}$	-	$4.683780 \cdot 10^{1}$	-
2	$2.106274 \cdot 10^{-1}$	1.2349	$1.432574 \cdot 10^{1}$	1.6550
3	$1.158169 \cdot 10^{-1}$	0.8492	$4.556323 \cdot 10^{0}$	1.6266
X_n in $\overline{\Omega}^{pm}$				
mesh number	error l_2	EOC l_2	error l_1	EOC l_1
1	$1.459467 \cdot 10^{-4}$	-	$4.720607 \cdot 10^{-3}$	-
2	$8.260621 \cdot 10^{-5}$	0.7952	$2.363393 \cdot 10^{-3}$	0.9666
3	$3.492286 \cdot 10^{-5}$	1.2225	$6.727359 \cdot 10^{-4}$	1.7842
T in $\overline{\Omega}^{pm}$				
mesh number	error l_2	EOC l_2	error l_1	EOC l_1
1	$8.252852 \cdot 10^{-3}$	-	$1.469128 \cdot 10^{-1}$	-
2	$6.480628 \cdot 10^{-3}$	0.3377	$1.115703 \cdot 10^{-1}$	0.3845
3	$3.396655 \cdot 10^{-3}$	0.9173	$5.671265 \cdot 10^{-2}$	0.9608

Table 4: Errors and experimental orders of convergence (EOCs) for $\overline{\Omega}^{ff}$ for Test 1.

ρ in $\overline{\Omega}^{ff}$				
mesh number	error l_2	EOC l_2	error l_1	EOC l_1
1	$4.291818 \cdot 10^{-3}$	-	$7.287217 \cdot 10^{-2}$	-
2	$2.316371 \cdot 10^{-3}$	0.8616	$2.469543 \cdot 10^{-2}$	1.5118
3	$8.281412 \cdot 10^{-4}$	1.4605	$6.630573 \cdot 10^{-3}$	1.8671
ρ_n in $\overline{\Omega}^{ff}$				
mesh number	error l_2	EOC l_2	error l_1	EOC l_1
1	$2.316029 \cdot 10^{-4}$	-	$4.576338 \cdot 10^{-3}$	-
2	$1.914159 \cdot 10^{-4}$	0.2662	$2.411136 \cdot 10^{-3}$	0.8952
3	$7.477627 \cdot 10^{-5}$	1.3347	$5.245653 \cdot 10^{-4}$	2.1658
ρv_1 in $\overline{\Omega}^{ff}$				
mesh number	error l_2	EOC l_2	error l_1	EOC l_1
1	$3.031204 \cdot 10^{-2}$	-	$5.576193 \cdot 10^{0}$	-
2	$6.931596 \cdot 10^{-3}$	2.0613	$1.275801 \cdot 10^{0}$	2.0606
3	$1.621265 \cdot 10^{-3}$	2.0630	$2.693425 \cdot 10^{-1}$	2.2085

Table 4 (continued).

ρv_2 in $\overline{\Omega}^{ff}$				
mesh number	error l_2	EOC l_2	error l_1	EOC l_1
1	$6.259461 \cdot 10^{-4}$	-	$1.568492 \cdot 10^{-2}$	-
2	$3.692922 \cdot 10^{-4}$	0.7372	$6.882566 \cdot 10^{-3}$	1.1508
3	$1.555041 \cdot 10^{-4}$	1.2281	$2.059193 \cdot 10^{-3}$	1.7134
ρe in $\overline{\Omega}^{ff}$				
mesh number	error l_2	EOC l_2	error l_1	EOC l_1
1	$1.349656 \cdot 10^{1}$	-	$3.278175 \cdot 10^{2}$	-
2	$8.967213 \cdot 10^{0}$	0.5712	$1.382702 \cdot 10^{2}$	1.2060
3	$3.501076 \cdot 10^{0}$	1.3355	$3.111505 \cdot 10^{1}$	2.1179

4.1.2 Test 2

This test models the same situation as Test 1, but the algorithm from Section 3.4 is modified in the way described below. This test is performed in order to show that this modification can be done.

- Particular test setting: Same as in Test 1.
- Particular coupling conditions: Same as in Test 1, except that for this test, the algorithm from Section 3.4 is modified so that on each time interval $[t_n, t_{n+1}]$, the submodel from Section 3.1 is solved prior to the submodel from Section 3.2.

The resulting errors and corresponding EOC coefficients are listed in Tables 5 and 6, pages 376 and 377. As expected, they are very similar to the results of Test 1.

4.1.3 Test 3

This test is similar to Test 1. But in this case, the NAPL vapor penetrates the soil which is cooled. Moreover, we use a different combination of coupling conditions.

- Particular test setting: $T_0^{pm} = 295.65$, $X_{n,0}^{pm} = 0$, $T_0^{ff} = 295.15$, $v_{1,0} = 10.0$, $p_1 = p_0$, $p_2 = 101315.0$, $X_{n,0}^{ff} = 10^{-3}$ and $X_{n,1} = X_{n,0}^{ff}$. The soil is homogeneous. Its properties correspond to the parameter values with the subscript 1 in Table 1, page 369.
- Particular coupling conditions: Condition (2.35) is used for the mass fraction of the NAPL vapor X_n in (2.11). Condition (2.41) is used for the mass flux of the NAPL vapor in (2.20).

The resulting errors and corresponding EOC coefficients are listed in Tables 7 and 8, pages 377 and 378.

Table 5: Errors and experimental orders of convergence (EOCs) for $\overline{\Omega}^{pm}$ for Test 2.

p in $\overline{\Omega}^{pm}$				
mesh number	error l_2	EOC l_2	error l_1	EOC l_1
1	$5.097926\cdot10^{-1}$	-	$4.684219\cdot10^{1}$	-
2	$2.106699\cdot10^{-1}$	1.2346	$1.432051\cdot10^{1}$	1.6557
3	$1.263277\cdot10^{-1}$	0.7262	$4.462936\cdot10^{0}$	1.6555
X_n in $\overline{\Omega}^{pm}$				
mesh number	error l_2	EOC l_2	error l_1	EOC l_1
1	$1.458403\cdot10^{-4}$	-	$4.705354\cdot10^{-3}$	-
2	$8.255578\cdot10^{-5}$	0.7950	$2.361648\cdot10^{-3}$	0.9631
3	$3.498405\cdot10^{-5}$	1.2191	$6.726280\cdot10^{-4}$	1.7833
T in $\overline{\Omega}^{pm}$				
mesh number	error l_2	EOC l_2	error l_1	EOC l_1
1	$8.252334\cdot10^{-3}$	-	$1.468319\cdot10^{-1}$	-
2	$6.480188\cdot10^{-3}$	0.3377	$1.115312\cdot10^{-1}$	0.3842
3	$3.396360\cdot10^{-3}$	0.9173	$5.670170\cdot10^{-2}$	0.9606

Table 6: Errors and experimental orders of convergence (EOCs) for $\overline{\Omega}^{ff}$ for Test 2.

ρ in $\overline{\Omega}^{ff}$				
mesh number	error l_2	EOC l_2	error l_1	EOC l_1
1	$4.292611\cdot10^{-3}$	-	$7.286870\cdot10^{-2}$	-
2	$2.315768\cdot10^{-3}$	0.8622	$2.469129\cdot10^{-2}$	1.5119
3	$8.276825\cdot10^{-4}$	1.4609	$6.627576\cdot10^{-3}$	1.8675
ρ_n in $\overline{\Omega}^{ff}$				
mesh number	error l_2	EOC l_2	error l_1	EOC l_1
1	$2.310381\cdot10^{-4}$	-	$4.574550\cdot10^{-3}$	-
2	$1.911726\cdot10^{-4}$	0.2646	$2.410002\cdot10^{-3}$	0.8954
3	$7.469858\cdot10^{-5}$	1.3343	$5.240306\cdot10^{-4}$	2.1666
ρv_1 in $\overline{\Omega}^{ff}$				
mesh number	error l_2	EOC l_2	error l_1	EOC l_1
1	$3.062718\cdot10^{-2}$	-	$5.576724\cdot10^{0}$	-
2	$6.963459\cdot10^{-3}$	2.0694	$1.275689\cdot10^{0}$	2.0608
3	$1.595353\cdot10^{-3}$	2.0924	$2.693916\cdot10^{-1}$	2.2081

Table 6 (continued).

ρv_2 in $\overline{\Omega}^{ff}$				
mesh number	error l_2	EOC l_2	error l_1	EOC l_1
1	$6.259481\cdot10^{-4}$	-	$1.568834\cdot10^{-2}$	-
2	$3.692939\cdot10^{-4}$	0.7372	$6.882376\cdot10^{-3}$	1.1511
3	$1.555051\cdot10^{-4}$	1.2281	$2.058395\cdot10^{-3}$	1.7139
ρe in $\overline{\Omega}^{ff}$				
mesh number	error l_2	EOC l_2	error l_1	EOC l_1
1	$1.372076\cdot10^{1}$	-	$3.276810\cdot10^{2}$	-
2	$8.963384\cdot10^{0}$	0.5948	$1.384656\cdot10^{2}$	1.2035
3	$3.501324\cdot10^{0}$	1.3347	$3.118421\cdot10^{1}$	2.1167

Table 7: Errors and experimental orders of convergence (EOCs) for $\overline{\Omega}^{pm}$ for Test 3.

p in $\overline{\Omega}^{pm}$				
mesh number	error l_2	EOC l_2	error l_1	EOC l_1
1	$5.271308\cdot10^{-1}$	-	$4.796027\cdot10^{1}$	-
2	$2.174821\cdot10^{-1}$	1.2369	$1.425991\cdot10^{1}$	1.6945
3	$1.021158\cdot10^{-1}$	1.0735	$4.285839\cdot10^{0}$	1.7070
X_n in $\overline{\Omega}^{pm}$				
mesh number	error l_2	EOC l_2	error l_1	EOC l_1
1	$1.485054\cdot10^{-4}$	-	$6.205378\cdot10^{-3}$	-
2	$8.210769\cdot10^{-5}$	0.8279	$1.771374\cdot10^{-3}$	1.7515
3	$3.231605\cdot10^{-5}$	1.3240	$5.233401\cdot10^{-4}$	1.7313
T in $\overline{\Omega}^{pm}$				
mesh number	error l_2	EOC l_2	error l_1	EOC l_1
1	$8.383680\cdot10^{-4}$	-	$1.584700\cdot10^{-2}$	-
2	$6.552652\cdot10^{-4}$	0.3443	$1.173008\cdot10^{-2}$	0.4203
3	$3.386718\cdot10^{-4}$	0.9372	$5.913397\cdot10^{-3}$	0.9726

Table 8: Errors and experimental orders of convergence (EOCs) for $\overline{\Omega}^{ff}$ for Test 3.

ρ in $\overline{\Omega}^{ff}$				
mesh number	error l_2	EOC l_2	error l_1	EOC l_1
1	$4.619816\cdot10^{-4}$	-	$8.821972\cdot10^{-3}$	-
2	$2.476805\cdot10^{-4}$	0.8709	$2.730564\cdot10^{-3}$	1.6384
3	$9.121167\cdot10^{-5}$	1.4185	$7.845394\cdot10^{-4}$	1.7709

Table 8 (continued).

ρ_n in $\overline{\Omega}^{ff}$				
mesh number	error l_2	EOC l_2	error l_1	EOC l_1
1	$7.440048\cdot10^{-5}$	-	$2.446830\cdot10^{-3}$	-
2	$4.374683\cdot10^{-5}$	0.7419	$9.565878\cdot10^{-4}$	1.3121
3	$2.027859\cdot10^{-5}$	1.0917	$2.982784\cdot10^{-4}$	1.6547
ρv_1 in $\overline{\Omega}^{ff}$				
mesh number	error l_2	EOC l_2	error l_1	EOC l_1
1	$1.463711\cdot10^{-2}$	-	$2.776736\cdot10^{0}$	-
2	$3.653551\cdot10^{-3}$	1.9389	$6.358227\cdot10^{-1}$	2.0594
3	$8.278029\cdot10^{-4}$	2.1081	$1.337722\cdot10^{-1}$	2.2134
ρv_2 in $\overline{\Omega}^{ff}$				
mesh number	error l_2	EOC l_2	error l_1	EOC l_1
1	$4.366362\cdot10^{-4}$	-	$1.111823\cdot10^{-2}$	-
2	$3.726740\cdot10^{-4}$	0.2213	$5.709312\cdot10^{-3}$	0.9311
3	$2.162009\cdot10^{-4}$	0.7731	$2.815189\cdot10^{-3}$	1.0040
ρe in $\overline{\Omega}^{ff}$				
mesh number	error l_2	EOC l_2	error l_1	EOC l_1
1	$3.486931\cdot10^{0}$	-	$1.453591\cdot10^{2}$	-
2	$2.067647\cdot10^{0}$	0.7301	$5.235062\cdot10^{1}$	1.4268
3	$9.583252\cdot10^{-1}$	1.0919	$1.618243\cdot10^{1}$	1.6671

4.1.4 Test 4

This test models a situation similar to that in Test 3. But in this case, the mixture entering Ω^{ff} from the left differs from the mixture inside Ω^{ff} in ρ, ρ_n and T. Moreover, the soil is heterogeneous.

- Particular test setting: $T_0^{pm}=296.15$, $X_{n,0}^{pm}=0$, $T_0^{ff}=295.15$, $v_{1,0}=20.0$, $p_1=101525.0$, $p_2=101315.0$, $X_{n,0}^{ff}=0$ and $X_{n,1}=10^{-3}$. Inside Ω^{pm}, there are three regions of low permeability the boundary of which are depicted in Fig. 7, page 380. In Table 1 (page 369), the subscripts 1 and 2 correspond to the parameters of the soil with the higher and lower permeability, respectively.

- Particular coupling conditions: Same as in Test 1.

The resulting errors and corresponding EOC coefficients are listed in Tables 9 and 10, pages 379 and 380. Fig. 7 (page 380) also depicts the direction of the flow and the pressure distribution in Ω.

Table 9: Errors and experimental orders of convergence (EOCs) for $\overline{\Omega}^{pm}$ for Test 4.

p in $\overline{\Omega}^{pm}$				
mesh number	error l_2	EOC l_2	error l_1	EOC l_1
1	$7.620412\cdot10^{-1}$	-	$9.284969\cdot10^{1}$	-
2	$2.651467\cdot10^{-1}$	1.4749	$2.297277\cdot10^{1}$	1.9513
3	$9.077255\cdot10^{-2}$	1.5221	$6.959354\cdot10^{0}$	1.6957
X_n in $\overline{\Omega}^{pm}$				
mesh number	error l_2	EOC l_2	error l_1	EOC l_1
1	$9.926345\cdot10^{-5}$	-	$2.743497\cdot10^{-3}$	-
2	$5.524305\cdot10^{-5}$	0.8187	$9.683046\cdot10^{-4}$	1.4550
3	$1.501800\cdot10^{-5}$	1.8495	$2.402539\cdot10^{-4}$	1.9792
T in $\overline{\Omega}^{pm}$				
mesh number	error l_2	EOC l_2	error l_1	EOC l_1
1	$1.933644\cdot10^{-3}$	-	$2.985016\cdot10^{-2}$	-
2	$1.518990\cdot10^{-3}$	0.3372	$2.297951\cdot10^{-2}$	0.3655
3	$8.132838\cdot10^{-4}$	0.8871	$1.177145\cdot10^{-2}$	0.9498

Table 10: Errors and experimental orders of convergence (EOCs) for $\overline{\Omega}^{ff}$ for Test 4.

ρ in $\overline{\Omega}^{ff}$				
mesh number	error l_2	EOC l_2	error l_1	EOC l_1
1	$8.610408\cdot10^{-4}$	-	$1.790453\cdot10^{-2}$	-
2	$4.601266\cdot10^{-4}$	0.8755	$6.228124\cdot10^{-3}$	1.4753
3	$1.682407\cdot10^{-4}$	1.4286	$1.972030\cdot10^{-3}$	1.6329
ρ_n in $\overline{\Omega}^{ff}$				
mesh number	error l_2	EOC l_2	error l_1	EOC l_1
1	$1.638326\cdot10^{-4}$	-	$6.752006\cdot10^{-3}$	-
2	$8.870314\cdot10^{-5}$	0.8572	$2.843319\cdot10^{-3}$	1.2083
3	$3.841112\cdot10^{-5}$	1.1884	$8.482763\cdot10^{-4}$	1.7174
ρv_1 in $\overline{\Omega}^{ff}$				
mesh number	error l_2	EOC l_2	error l_1	EOC l_1
1	$2.928273\cdot10^{-2}$	-	$5.568479\cdot10^{0}$	-
2	$6.703896\cdot10^{-3}$	2.0597	$1.267855\cdot10^{0}$	2.0674
3	$1.477936\cdot10^{-3}$	2.1470	$2.675459\cdot10^{-1}$	2.2091

Table 10 (continued).

ρv_2 in $\overline{\Omega}^{ff}$				
mesh number	error l_2	EOC l_2	error l_1	EOC l_1
1	$2.572633 \cdot 10^{-4}$	-	$1.217678 \cdot 10^{-2}$	-
2	$2.036363 \cdot 10^{-4}$	0.3266	$7.040056 \cdot 10^{-3}$	0.7655
3	$1.344821 \cdot 10^{-4}$	0.5891	$3.097830 \cdot 10^{-3}$	1.1656
ρe in $\overline{\Omega}^{ff}$				
mesh number	error l_2	EOC l_2	error l_1	EOC l_1
1	$7.859271 \cdot 10^{0}$	-	$4.322761 \cdot 10^{2}$	-
2	$4.231543 \cdot 10^{0}$	0.8650	$1.606827 \cdot 10^{2}$	1.3826
3	$1.830714 \cdot 10^{0}$	1.1897	$4.574894 \cdot 10^{1}$	1.7838

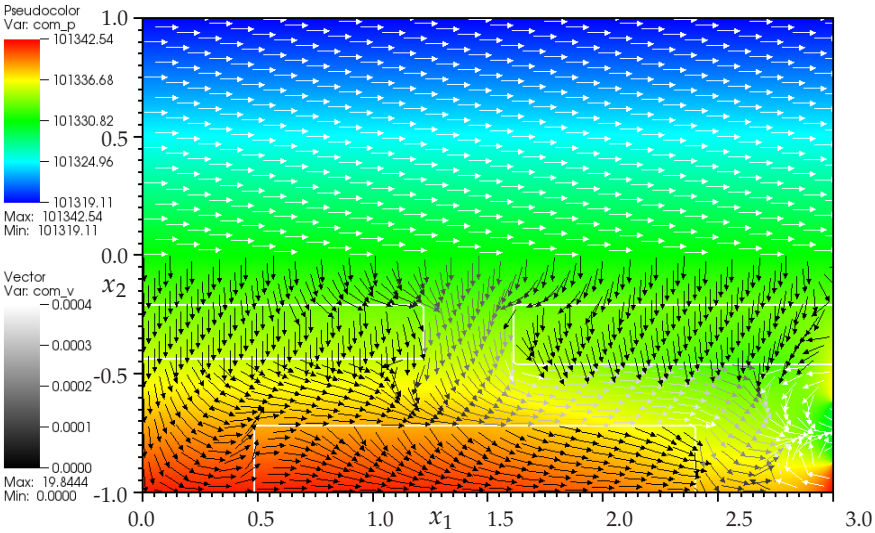

Figure 7: Test 4: Pressure p [Pa] and velocity field at time 2.0 s which were considered as the fine solution. The arrows indicate the direction and magnitude of the velocity v $[\mathrm{m \cdot s^{-1}}]$. The gray lines are the boundaries of the regions of low permeability.

4.1.5 Discussion of results

The resulting errors and corresponding EOC coefficients are listed in Tables 3–10 (pages 374–380), where the EOC coefficient in the i-th row is calculated from the errors on the $(i-1)$-th and i-th mesh.

Although on each mesh, the numerical approximations of the line segment $\Gamma^{pm}_{\mathrm{gap}_2}$ and the regions of low permeability differ, the EOC coefficients indicate the convergence of the numerical solution.

The values of the EOC coefficients for T are influenced by longer relaxation times of

heat transfer inside soil. However, due to the runtimes listed on page 373, simulations with t_{fin}, e.g., of the order of hours or days are beyond the scope of this paper. The reason why the EOC coefficients for ρv_2 are much lower than that for ρv_1 may be the fact that ρv_2 is much more affected by the presence of the artificial interface between Ω^{ff} and Ω^{pm} near which the values of ρv_2 may oscillate. These possible oscillations then increase the error in the other variables on both sides of the interface $\mathcal{I}$.

This effect can be illustrated by the following example. If we measure the error in the numerical solution in Test 1 at the k-th mesh node as

$$\left\| z_h^k - z_{\text{fine}}^k \right\|_{\tilde{l}_2} = \sqrt{\sum_{j=0,\cdots,N} \nu \left| z_h^k(t_{\text{ini}}+j\nu) - z_{\text{fine}}^k(t_{\text{ini}}+j\nu) \right|^2}, \tag{4.8}$$

where we use the same notation as in Eqs. (4.4)–(4.6), and compare the resulting values, we can see that the largest error in ρv_2 and, e.g., in X_n occurs indeed near the interface $\mathcal{I}$. This is depicted in Figs. 8 and 9.

Tests 1–4 also show the following important details: Tests 1 and 2 prove that in the algorithm from Section 3.4, the submodels from Sections 3.1 and 3.2 can be solved in reverse order. Further, Tests 3 and 4 prove that we can use both combinations of coupling conditions listed in Section 2.3.

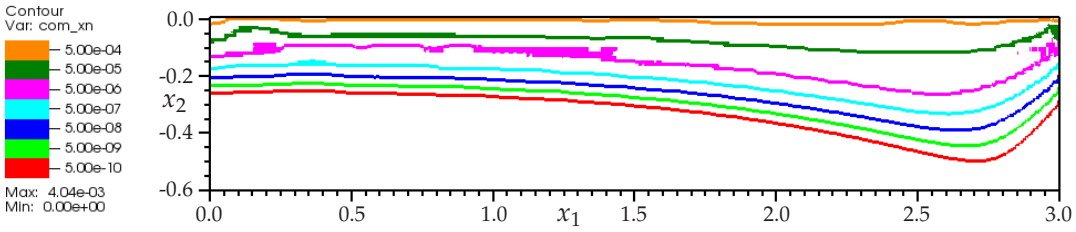

Figure 8: Test 1: Contour lines of the error (in the $\tilde{l}_2$-norm) in the mass fraction of NAPL vapor X_n calculated on mesh 3. The highest error occurs near the interface $\mathcal{I}$, which is located at $x_2 = 0.0$. Only the part of Ω^{pm} for $x_2 \geq -0.6$ is shown because in the rest of Ω^{pm}, the error is lower than $5 \cdot 10^{-10}$.

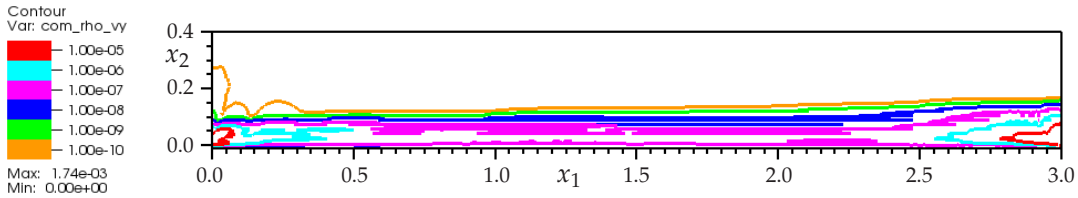

Figure 9: Test 1: Contour lines of the error (in the $\tilde{l}_2$-norm) in the momentum component ρv_2 calculated on mesh 3. The largest error occurs near the interface $\mathcal{I}$, which is located at $x_2 = 0.0$. Only the part of Ω^{ff} for $x_2 \leq 0.4$ is shown because in the rest of Ω^{ff}, the error is lower than 10^{-10}.

4.2 Qualitative computational studies

In this section, we present the results of three tests (Tests 5–7) with a longer time interval $[t_{\text{ini}}, t_{\text{fin}}]$. In all of these tests, we chose $t_{\text{ini}} = 0$, $t_{\text{fin}} = 24 \cdot 3600$ and we employed the same spatial meshes and time steps τ and τ_{cou} as in the case of the mesh 1 in Section 4.1.

4.2.1 Test 5

This test models the penetration of NAPL vapor into a tank filled with heterogeneous soil under the cooling of this soil in the case where the gaseous mixture is pumped out of the tank through a gap in one of its walls.

- Division of $\partial\Omega$: As in Fig. 5b, page 370.
- Particular test setting: $T_0^{pm} = 296.15$, $X_{n,0}^{pm} = 0$, $T_0^{ff} = 295.15$, $v_{1,0} = 20.0$, $p_1 = 101525.0$, $X_{n,0}^{ff} = 0$ and $X_{n,1} = 10^{-3}$. The soil properties are the same as in Test 4.
- Particular coupling conditions: Same as in Test 3.

The results are depicted in Figs. 10 and 11, pages 382 and 383. We can see that the changes in X_n inside Ω^{pm} are much faster than the changes in T.

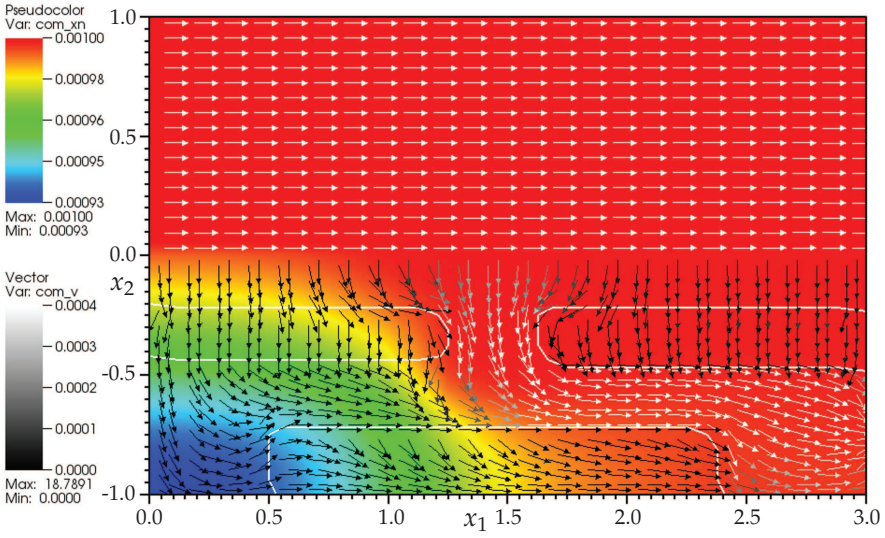

Figure 10: Test 5: Mass fraction X_n $[-]$ and velocity field at time 24 h. The arrows indicate the direction and magnitude of the velocity v $[\text{m}\cdot\text{s}^{-1}]$. The gray lines are the boundaries of the regions of low permeability. The color scale indicates that the spatial distribution of X_n in Ω^{pm} is determined by the shapes of these regions and by the gap in the right wall. It also indicates that after 24 h, X_n is almost constant in Ω.

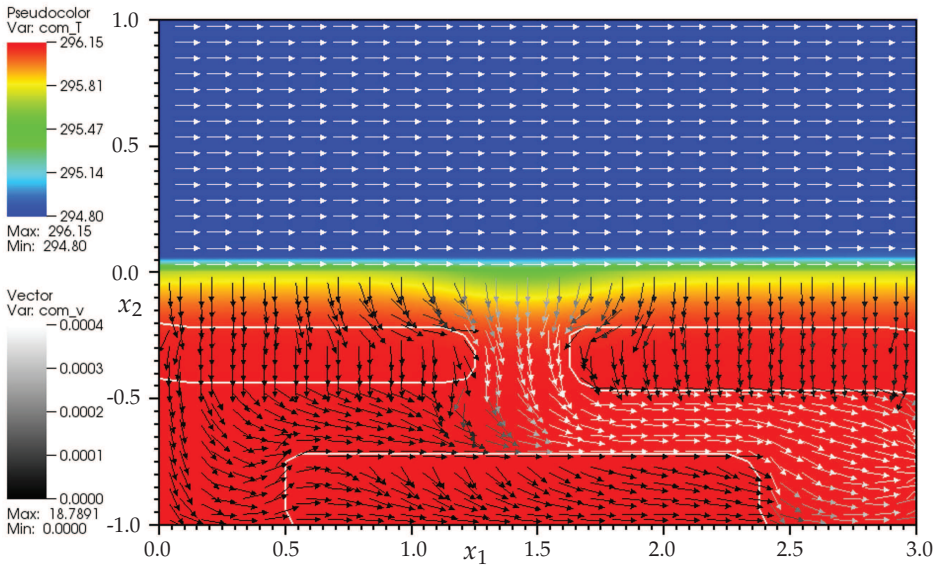

Figure 11: Test 5: Temperature T [K] and velocity field at time 24 h. The arrows indicate the direction and magnitude of the velocity v $[\mathrm{m}\cdot\mathrm{s}^{-1}]$. The gray lines are the boundaries of the regions of low permeability. The color scale indicates that after 24 h, the spatial distribution of T is almost the same as the initial one (cf. Fig. 10, page 382), and that the soil cools the fastest near the middle of the interface $\mathcal{I}$ (i.e., near the gap among the regions of low permeability).

4.2.2 Test 6

This test models the escape of NAPL vapor from a tank filled with homogeneous soil. Contrary to Test 5, the walls of the tank are perfectly sealed.

- Division of $\partial\Omega$: As in Fig. 4, page 370, except that $\Gamma^{pm}_{\mathrm{gap}_1}$ is replaced by $\Gamma^{pm}_{\mathrm{wall}}$.
- Particular test setting: $T^{pm}_0 = 290.15$, $X^{pm}_{n,0} = 10^{-3}$, $T^{ff}_0 = 295.15$, $v_{1,0} = 20.0$, $p_1 = p_0$, $X^{ff}_{n,0} = 0$ and $X_{n,1} = 0$. The soil properties are the same as in Test 1.
- Particular coupling conditions: Same as in Test 1.

The results are depicted in Figs. 12, 13 and 14, pages 384 and 385. In the first two figures, we can see how the NAPL vapor gradually escapes from Ω, and how Ω^{pm} slowly warms up. The graph in Fig. 14 shows how the escaping rate of the NAPL vapor decreases in time, which agrees with the results of the physical experiments presented in [26].

4.2.3 Test 7

This test models the heating of cold air above the surface of warm soil.

- Division of $\partial\Omega$: As in Fig. 6, page 371.

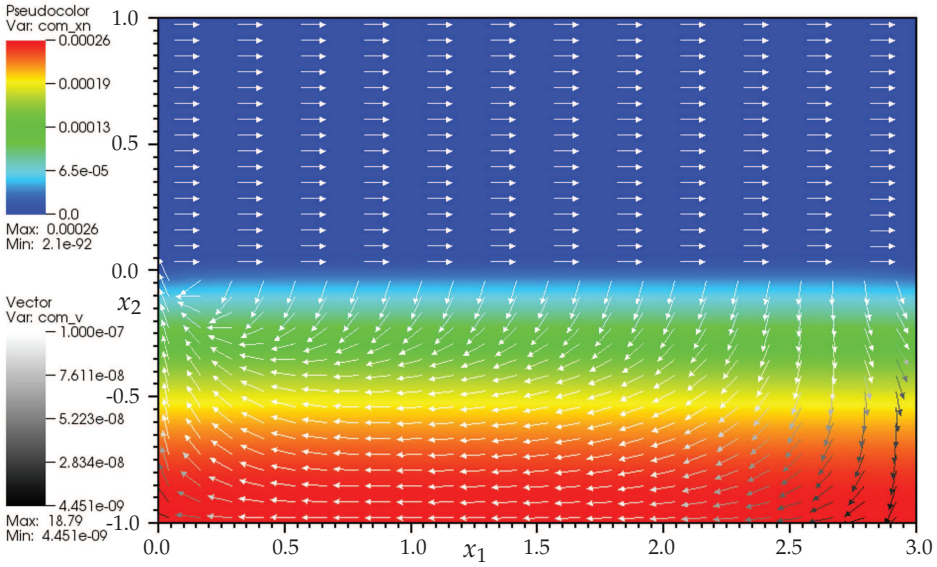

Figure 12: Test 6: Mass fraction X_n $[-]$ and velocity field at time 24 h. The arrows indicate the direction and magnitude of the velocity v $[\mathrm{m}\cdot\mathrm{s}^{-1}]$. The color scale indicates that the distribution of X_n in Ω^{pm} is almost uniform in x_1 direction, and that the NAPL vapor gradually escapes from Ω (the initial value of X_n in Ω^{pm} was 10^{-3}).

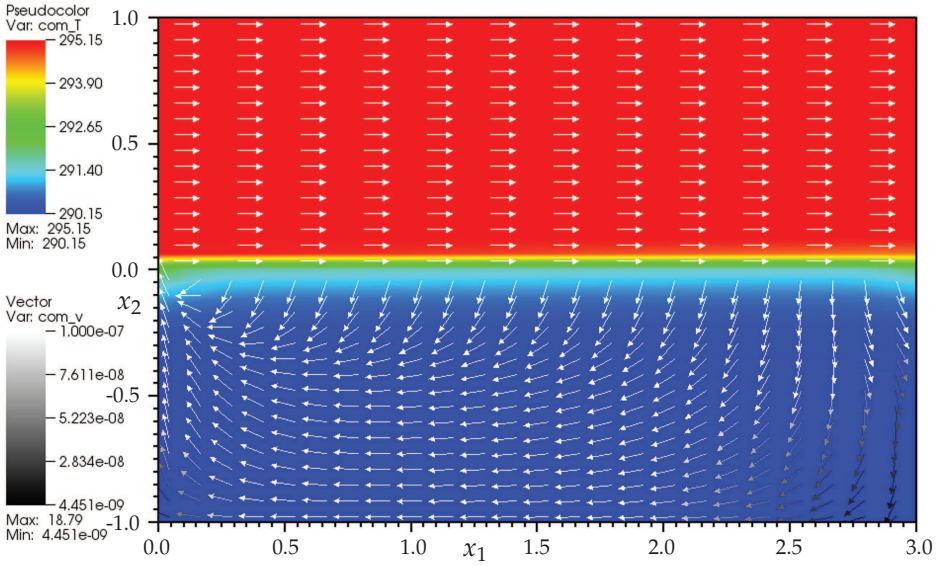

Figure 13: Test 6: Temperature T $[\mathrm{K}]$ and velocity field at time 24 h. The arrows indicate the direction and magnitude of the velocity v $[\mathrm{m}\cdot\mathrm{s}^{-1}]$. From the color scale, it follows that after 24 h, the highest increase in T occurs near the ends of the interface $\mathcal{I}$. However, the values of T are still very similar to the initial ones (cf. Fig. 12).

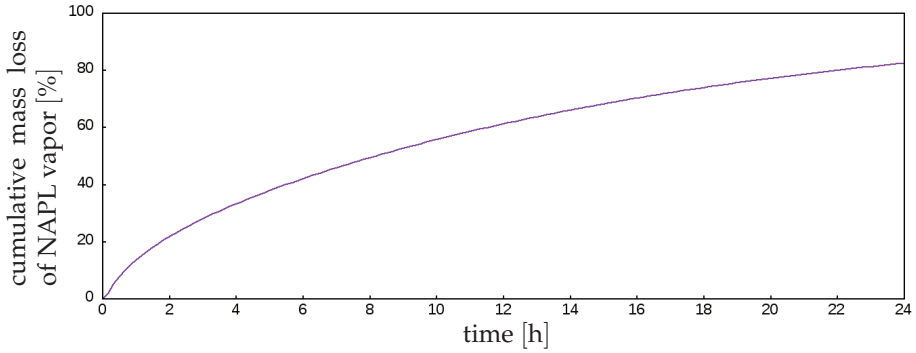

Figure 14: Test 6: Cumulative mass loss of NAPL vapor from Ω during the simulation. The NAPL vapor gradually escapes from Ω, and its escaping rate decreases in time, which agrees with the results presented in [26].

- Particular test setting: $T_0^{pm} = 305.15$, $X_{n,0}^{pm} = 0$, $T_0^{ff} = 295.15$, $X_{n,0}^{ff} = 0$ and $\boldsymbol{v}_{1,0} = 0$. The soil properties are the same as in Test 1.

- Particular coupling conditions: Same as in Test 1.

In Fig. 15 (page 386) we can see the chaotic behavior of the flow field in this test. From the color scale, it follows that Ω^{ff} warms up, but the temperature in Ω^{pm} remains almost the same.

5 Conclusions

In this paper, we proposed a mathematical formulation and a numerical model for the description of the non-isothermal compressible flow of a mixture of two gases in a heterogeneous porous medium and the atmospheric boundary layer above its surface. Our model proves to be able to simulate the gas exchange between these two flow domains under the cooling or heating of the porous medium with realistic material properties. It also proves to be able to simulate the heating of the atmospheric boundary layer by a warm porous medium.

Further, we verified the convergence of our numerical algorithm by means of the measurement of the experimental order of convergence on several test problems.

At this stage, however, only the model and its applicability to hypothetical scenarios with realistic material properties are presented. It is our future goal to generate data in a coupled porous media/wind tunnel facility that is available to the authors to validate the model.

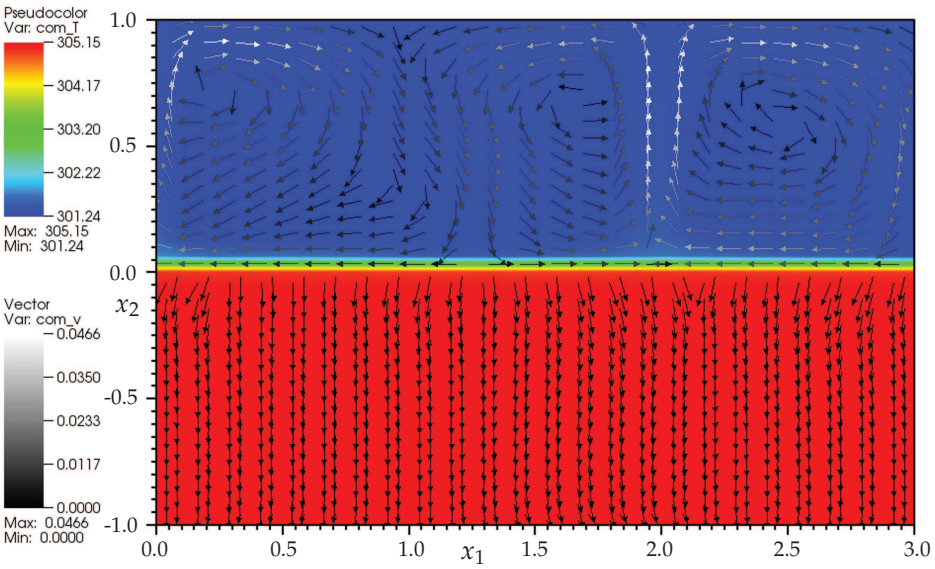

(a) Time $t = 40$ min.

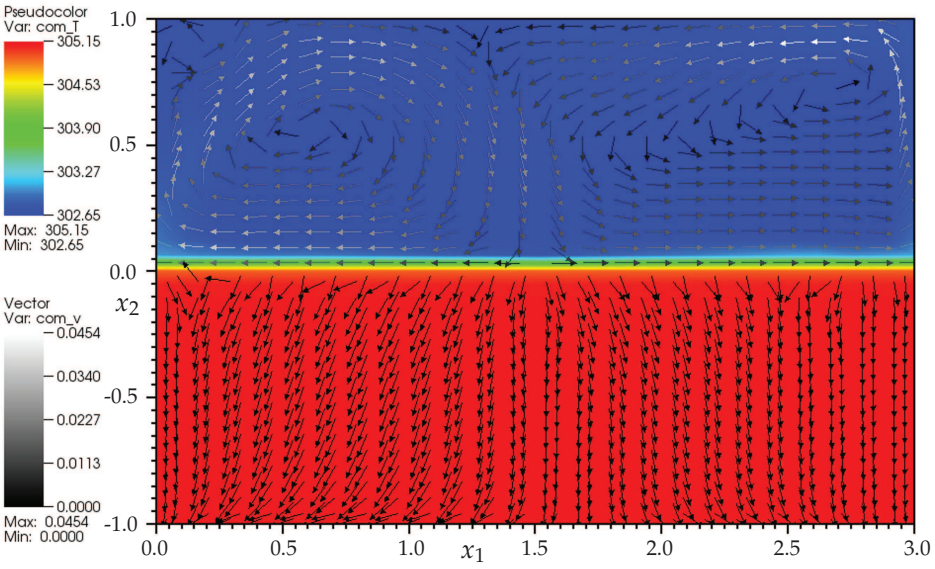

(b) Time $t = 1$ h.

Figure 15: Test 7: Temperature T [K] and velocity field at different times. The arrows indicate the direction and magnitude of the velocity v $[\mathrm{m}\cdot\mathrm{s}^{-1}]$. The flow in Ω^{ff} induced by the warm soil is very chaotic, which greatly accelerates heat transfer in Ω^{ff}. (The initial T in Ω^{ff} was 295.15.) From the color scales, we can see that despite the rapid increase in T in Ω^{ff}, the values of T in Ω^{pm} remain almost the same (cf. Figs 11 and 13, pages 383 and 384).

Acknowledgments

The first three authors were supported by the project "Investigation of shallow subsurface flow with phase transitions" number 17-06759S of the Czech Science Foundation and by the project "Application of advanced supercomputing methods for mathematical modeling of natural processes" number SGS17/194/OHK4/3T/14 of the Student Grant Agency of the Czech Technical University in Prague. The fourth author acknowledges the support of the Strategic Environmental Research and Development Program Grant ER-1687.

References

[1] K. Baber, K. Mosthaf, B. Flemisch, R. Helmig, S. Müthing, and B. Wohlmuth. Numerical scheme for coupling two-phase compositional porous-media flow and one-phase compositional free flow. *IMA J. Appl. Math.*, 887–909, 2012.
[2] L. Badea, M. Discacciati, and A. Quarteroni. Numerical analysis of the Navier–Stokes/Darcy coupling. *Numerische Mathematik*, 115(2):195–227, 2010.
[3] A. Bejan. *Convection Heat Transfer*. John Wiley & Sons, Inc., 4th edition, 2013.
[4] J. Blazek. *Computational Fluid Dynamics*. Elsevier, 2001.
[5] T. Carraro, C. Goll, A. Marciniak-Czochra, and A. Mikelić. Pressure jump interface law for the Stokes–Darcy coupling: confirmation by direct numerical simulations. *J. Fluid Mech.*, 732:510–536, 2013.
[6] S. Chapman and T. G. Cowling. *The Mathematical Theory of Non-Uniform Gases*. Cambridge University Press, 2nd edition, 1952.
[7] J. Chen, S. Sun, and X.-P. Wang. A numerical method for a model of two-phase flow in a coupled free flow and porous media system. *J. Comput. Phys.*, 268:1–16, 2014.
[8] H. Davarzani, K. Smits, R. M. Tolene, and T. Illangasekare. Study of the effect of wind speed on evaporation from soil through integrated modeling of the atmospheric boundary layer and shallow subsurface. *Water Resour. Res.*, 50(1):661–680, 2014.
[9] T. A. Davis. Algorithm 832: UMFPACK V4.3—an unsymmetric-pattern multifrontal method. *ACM Trans. Math. Softw.*, 30(2):196–199, 2004.
[10] K. Deckelnick, G. Dziuk, and C. M. Elliott. Computation of geometric partial differential equations and mean curvature flow. *Acta Numerica*, 14:139–232, 5 2005.
[11] A. Dereims, S. Drapier, J.-M. Bergheau, and P. De Luca. 3D robust iterative coupling of Stokes, Darcy and solid mechanics for low permeability media undergoing finite strains. *Finite Elem. Anal. Des.*, 94:1–15, 2015.
[12] J. H. Ferziger and H. G. Kaper. *Mathematical Theory of Transport Processes in Gases*. North-Holland Publishing Company, 1st edition, 1972.
[13] T. Fetzer, K. M. Smits, and R. Helmig. Effect of turbulence and roughness on coupled porous-medium/free-flow exchange processes. *Transp. Porous Media*, 114(2):395–424, 2016.
[14] D. Folkes, W. Wertz, J. Kurtz, and T. Kuehster. Observed spatial and temporal distributions of CVOCs at Colorado and New York vapor intrusion sites. *Ground Water Monit. Rem.*, 29(1):70–80, 2009.
[15] P. Frolkovič and H. D. Schepper. Numerical modelling of convection dominated transport coupled with density driven flow in porous media. *Adv. Water Resour.*, 24(1):63–72, 2000.
[16] V. Giovangigli. *Multicomponent Flow Modeling*. Birkhäuser, Boston, 1st edition, 1999.

[17] M. Holodniok, A. Klíč, M. Kubíček, and M. Marek. *Methods of Analysis of Nonlinear Dynamical Models (in Czech)*. Academia, 1st edition, 1986.
[18] N. I. Kolev. *Multiphase Flow Dynamics 1*. Springer-Verlag, Berlin, 2nd edition, 2005.
[19] R. Masson, L. Trenty, and Y. Zhang. Coupling compositional liquid gas Darcy and free gas flows at porous and free-flow domains interface. *J. Comput. Phys.*, 321:708–728, 2016.
[20] K. Mosthaf, K. Baber, B. Flemisch, R. Helmig, A. Leijnse, I. Rybak, and B. Wohlmuth. A coupling concept for two-phase compositional porous-medium and single-phase compositional free flow. *Water Resour. Res.*, 47(10), 2011.
[21] D. A. Nield and A. Bejan. *Convection in Porous Media*. Springer, New York, 3rd edition, 2006.
[22] P. Pant and S. Pant. A review: Advances in microbial remediation of trichloroethylene (TCE). *J. Environ. Sci.*, 22(1):116–126, 2010.
[23] O. Pártl, M. Beneš, and P. Frolkovič. Finite volume scheme for modeling of NAPL vapor transport in air. In *Numerical Mathematics and Advanced Applications ENUMATH 2015*, 531–538. Springer International Publishing Switzerland, 2016.
[24] O. Pártl, M. Beneš, P. Frolkovič, T. Illangasekare, and K. Smits. Numerical modeling of non-isothermal gas flow and NAPL vapor transport in soil. *Comput. Phys. Commun.*, 202:175–187, 2016.
[25] S. Patankar. *Numerical Heat Transfer and Fluid Flow*. Taylor & Francis, 1980.
[26] B. G. Petri, R. Fučík, T. H. Illangasekare, K. M. Smits, J. A. Christ, T. Sakaki, and C. C. Sauck. Effect of NAPL source morphology on mass transfer in the vadose zone. *Groundwater*, 53(5):685–698, 2015.
[27] T. Sakaki and T. H. Illangasekare. Comparison of height-averaged and point-measured capillary pressure-saturation relations for sands using a modified tempe cell. *Water Resour. Res.*, 43(12), 2007.
[28] L. Shan, H. Zheng, and W. J. Layton. A decoupling method with different subdomain time steps for the nonstationary Stokes–Darcy model. *Numerical Methods for Partial Differential Equations*, 29(2):549–583, 2013.
[29] K. Soga, J. Page, and T. Illangasekare. A review of NAPL source zone remediation efficiency and the mass flux approach. *Journal of Hazardous Materials*, 110(1):13–27, 2004.
[30] N. Weatherill. Delaunay triangulation in computational fluid dynamics. *Comput. Math. Appl.*, 24(56):129–150, 1992.